



Delft University of Technology

Whole-Core 3D Multiphysics Transient Modeling of a Prismatic Micro High-Temperature Gas-Cooled Reactor

Van Den Berg, Marc C.; Lathouwers, Danny; Kloosterman, Jan Leen

DOI

[10.1080/00295450.2024.2426960](https://doi.org/10.1080/00295450.2024.2426960)

Publication date

2025

Document Version

Final published version

Published in

Nuclear Technology

Citation (APA)

Van Den Berg, M. C., Lathouwers, D., & Kloosterman, J. L. (2025). Whole-Core 3D Multiphysics Transient Modeling of a Prismatic Micro High-Temperature Gas-Cooled Reactor. *Nuclear Technology*, Article 2426960. <https://doi.org/10.1080/00295450.2024.2426960>

Important note

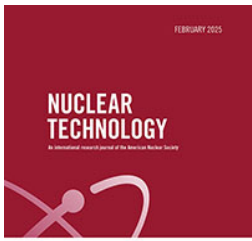
To cite this publication, please use the final published version (if applicable). Please check the document version above.

Copyright

Other than for strictly personal use, it is not permitted to download, forward or distribute the text or part of it, without the consent of the author(s) and/or copyright holder(s), unless the work is under an open content license such as Creative Commons.

Takedown policy

Please contact us and provide details if you believe this document breaches copyrights. We will remove access to the work immediately and investigate your claim.



Whole-Core 3D Multiphysics Transient Modeling of a Prismatic Micro High-Temperature Gas-Cooled Reactor

Marc C. Van Den Berg, Danny Lathouwers & Jan Leen Kloosterman

To cite this article: Marc C. Van Den Berg, Danny Lathouwers & Jan Leen Kloosterman (22 Jan 2025): Whole-Core 3D Multiphysics Transient Modeling of a Prismatic Micro High-Temperature Gas-Cooled Reactor, Nuclear Technology, DOI: [10.1080/00295450.2024.2426960](https://doi.org/10.1080/00295450.2024.2426960)

To link to this article: <https://doi.org/10.1080/00295450.2024.2426960>



© 2025 The Author(s). Published with license by Taylor & Francis Group, LLC.



Published online: 22 Jan 2025.



Submit your article to this journal [↗](#)



Article views: 114



View related articles [↗](#)



View Crossmark data [↗](#)



Whole-Core 3D Multiphysics Transient Modeling of a Prismatic Micro High-Temperature Gas-Cooled Reactor

Marc C. Van Den Berg,  Danny Lathouwers, * and Jan Leen Kloosterman

Delft University of Technology, Reactor Physics and Nuclear Materials Group, Mekelweg 15, 2629 JB Delft, The Netherlands

Received July 22, 2024

Accepted for Publication October 16, 2024

Abstract — *A three-dimensional whole-core transient coupled thermal-hydraulic and neutronics code system for modeling prismatic high-temperature gas-cooled reactors (HTGRs) is presented. The discrete ordinates method code PHANTOM- S_N was used to solve the multigroup neutron transport problem with cross sections generated with Serpent. The new finite element code OPERA was developed to solve the heat equation in the core and includes simplified subcodes for the coolant, reactor pressure vessel, and concrete containment building, as well as the power conversion cycle. Core graphite thermal conductivity degradation is included as a function of temperature and irradiation temperature. A 20-MW(thermal) HTGR design was modeled using the coupled multiphysics code to prove inherent safety. We simulated steady state, a depressurized loss of forced cooling (DLOFC), a partial blockage, and a reactivity insertion incident. We show that the DLOFC is not the most severe scenario for the fuel temperature in this prismatic micro HTGR. Upon a DLOFC, the peak fuel temperature remains well below the tri-structural isotropic (TRISO) fuel limits, even when the power is increased to 40 MW(thermal). However, during a partial blockage incident of one fuel assembly stack, the maximum fuel temperature reaches 2300°C, severely exceeding the limits. We furthermore contend that the graphite thermal conductivity values used in modeling should always be made explicit and that the temperature of irradiation should be included as a parameter since it can cause a sharp decrease (up to 97%) in the conductivity. We show that using unirradiated graphite parameters leads to an underestimation in peak temperature of 165°C while using a relatively low power density compared to other HTGRs. Finally, we argue that for prismatic HTGRs with a central reflector, bypass flow may lower the maximum fuel temperature.*

Keywords — *High-temperature gas-cooled reactor; multiphysics, transient modeling, passive safety, whole core.*

Note — *Some figures may be in color only in the electronic version.*

I. INTRODUCTION

For future energy supply, a promising opportunity is presented by inherently safe, long-lifetime, high-temperature

microreactors. Yet, exhaustively proving the inherent safety of a reactor by simulations remains a daunting task, even with today's computational resources. The task entails proving that the reactor can shut down passively during any given incident without exceeding the maximum design base temperature. This requires a transient whole-core coupled neutronics and thermal-hydraulic model that is both sufficiently fast to model the vastly different timescales during reactor transients and sufficiently detailed to model all relevant physics accurately. This task remains yet to be undertaken.

*E-mail: d.lathouwers@tudelft.nl

This is an Open Access article distributed under the terms of the Creative Commons Attribution License (<http://creativecommons.org/licenses/by/4.0/>), which permits unrestricted use, distribution, and reproduction in any medium, provided the original work is properly cited. The terms on which this article has been published allow the posting of the Accepted Manuscript in a repository by the author(s) or with their consent.

The model is often simplified to speed up computations, for instance, by lowering the spatial order. Most commonly, the assumption of cylindrical symmetry is made. Wols et al.^[1] simulated a depressurized loss of forced cooling (DLOFC) in a two-dimensional (2D) model of a pebble bed reactor that captures the distinct timescales at play. These range from seconds for fuel to start heating up because of the loss of cooling power, to hours for temperature-power oscillations upon recriticality, up to more than 100 h for the reactor to become stable after all ^{135}Xe decayed. However, the model does not include the finer temperature distribution of the pebbles, as 2D models can represent only a homogenized version of the core by assuming constant porosity.

Connolly et al.^[2] use the response-matrix method to model a prismatic high-temperature gas-cooled reactor (HTGR) in three dimensions, presenting a very detailed pin-level whole-core neutronics model. However, only steady-state simulations are shown. Huning et al.^[3] presented a whole-core thermal-hydraulic transient model (based on Ref. [4]), which captures transient core-level physics such as fuel and graphite temperatures, bypass flow, and heat redistribution after reactor SCRAM. A DLOFC was simulated, but only decay heat was considered, assuming an immediate scram. To prove the inherent safety of a reactor, a coupled model is necessary to capture the neutronics feedback, especially during recriticality after a DLOFC or a reactivity insertion incident.

Many papers exclude some aspect of the whole-core coupled transient studies. The transient studies may be excluded,^[5] assume a power distribution (e.g., a decay heat curve^[6]), or exclude neutronic calculations (e.g., see Refs. [7] and [8]). After an extensive literature study, only three papers were found that include whole-core coupled transient studies. In Refs. [9] and [10], Seubert et al. present results for a pebble bed reactor, where reactivity insertion events are modeled. However, the active core region is still modeled as a porous medium. The only work we are aware of showing whole-core transient analyses for a prismatic HTGR is that of Baier et al.^[11] They present their work on a control rod ejection. Moreover, they determine the temperature at a very detailed level, for the tri-structural isotropic (TRISO) kernel and its layers separately.

This is important because spatial homogenization of the temperature field between the fuel rod and the coolant channel is not conservative in two ways. First, the fuel temperatures are underestimated as the surrounding graphite is colder. But, perhaps more important is that the graphite temperature is, conversely,

overestimated. Irradiation temperature is the key parameter that determines the thermal conductivity of graphite.

Many models leave unmentioned how the thermal conductivity of graphite is determined. When it is mentioned, it is generally included as a function of dose or current temperature. In reality, however, irradiation damage causes the thermal conductivity to drop at an irradiation temperature-dependent rate. Especially at low temperature, graphite lattice defects that scatter heat-transporting phonons are immobile and can accumulate, causing the phonon mean free paths to drop dramatically. This can cause the thermal conductivity to decrease by a factor of 30.^[12] We are only aware of VSOP's (version 11/05) THERMIX^[13] code having an expression for the thermal conductivity that includes the irradiation temperature parameter. However, we have not found any paper explicitly mentioning the use of that expression.

To accurately compute the graphite temperature, a fine mesh is needed. To model individual fuel pins and the graphite lattice, the three-dimensional (3D) model's size is often reduced by making use of, e.g., 1/6th symmetry to compute the temperature at fuel pin level. The geometry reduction of models based on symmetry precludes simulating asymmetric transients. During a DLOFC, the entire core heats up, causing strong temperature feedback. Therefore, a DLOFC may constitute a relatively mild incident. This raises the following question: Does the nuclear reactor remain passively safe during incidents induced by local changes, such as a coolant channel blockage in only one fuel block?

This paper presents a transient whole-core coupled code for prismatic HTGRs, including a transient neutronics model and a thermal-hydraulic model with subpin-level resolution. The neutron transport equation is solved by the discrete ordinates code PHANTOM- S_N ^[14] with cross-section libraries precomputed in Serpent.^[15] The temperature is determined with the new in-house code OPERA, a finite element code that includes the thermal conductivity as a function of current and irradiation temperature, modules for determining the coolant and containment structure temperatures, and a simplified model of the power conversion cycle. To the best of our knowledge, we are the first to present a transient whole-core coupled model of an HTGR simulating a DLOFC or a partial blockage.

The two most important limitations of the model are the following. First, it is limited to smaller cores; we modeled a core with 120 fuel assemblies. Models up to approximately 1000 fuel assemblies are possible with enough memory (500 Gbytes). Second, bypass flow was

not included yet, although the paper includes a sensitivity analysis showing the effects.

We tested the model on a prismatic micro HTGR. Ding et al.^[16] devised a 20-MW(thermal) design that can operate over a period of more than 20 years without refueling by increasing the heterogeneity with a checkerboard-like pattern, lowering the resonance absorption. Section II describes the design. Section III introduces the Serpent-PHANTOM-S_N-OPERA code suite and the underlying theory. Section IV describes the coupling and simulation strategy. Section V analyses the simulated transients, which include a DLOFC, partial blockage, and a reactivity insertion incident. In addition, some sensitivity analyses of key assumptions are included. The conclusions of this unique 3D code system are discussed in Sec. VI.

II. REACTOR DESIGN

We tested the numerical model on a small and passively safe HTGR with a long core life. The reactor can provide power to off-grid electricity systems or industrial process heat. Ideally, the core lasts 20 years without refueling, and the reactor pressure vessel (RPV) is transportable by road. A high helium outlet temperature is desired for high-efficiency electricity generation or steam methane reforming, ranging from 750°C (like in Ref. [16]) up to 950°C, the limits for current material technology. To meet these requirements, Ding et al.^[16] researched different possible HTGR core layouts called the U-Battery®. This 20-MW(thermal) prismatic HTGR comprises four layers with 37 hexagonal fuel and moderator assemblies. It uses TRISO fuel particles that can withstand a temperature of at least 1600°C. The generally accepted safe steady-state maximum temperature limit is 1250°C (e.g., Ref. [17]). The design limit of the RPV is 395°C for steady state^[16] or 445°C for several hours during incidents.^[18]

Ding et al.^[16] researched incident scenarios for two different designs: a cylindrical layout where all 37×4 blocks are fuel assemblies and an annular layout where the 7 inner blocks at all four vertical layers are replaced by moderator assemblies. Their model showed that the maximum fuel temperature remains well below 1600°C in both designs. Furthermore, they found that the annular design has a lower maximum temperature and uses fuel more efficiently, making it the better design.

Ding et al.^[16] continued to optimize the design and proposed to distribute the 7×4 moderator blocks more evenly over the active core to increase the radial

heterogeneity. This composition extends the core lifetime to over 20 years without refueling with the following fuel parameters: an enrichment of 20%, a TRISO kernel size of 250 μm and a TRISO particle size of 510 μm, and a packing fraction of 30%. However, since the heterogeneity could not be modeled by Ding et al.'s 2D code, passive safety could not be verified.

The micro-HTGR core is shown on three different levels in Fig. 1. Figure 1a shows the fuel assembly developed for the Gas Turbine-Modular Helium Reactor (GT-MHR) project by General Atomics.^[19] The blocks are 36 cm flat-to-flat wide and 80 cm high and comprise a graphite matrix that is assumed isotropic, with 108 coolant channel and 216 fuel channel holes. The fuel pins consist of TRISO compacts with high-assay low-enriched uranium kernels and are held in place axially by graphite plugs of 3 cm.

Figure 1b depicts the active core of the longest-lifetime design as proposed by Ding et al.^[16] The radial distribution of the moderator blocks increases the resonance escape probability. The middle moderator block is surrounded by three rings, forming a 126-cm flat-to-flat-wide core. A 29-cm side reflector and 50-cm top and bottom reflectors surround the core. Figure 1c shows the silicon carbide (SiC) fiber thermal insulation of 10 cm at the sides and 100 cm at the top, which shields the barrel surrounding the core. Helium of 250°C flows upward in the gas gap between the barrel and the RPV, cooling the steel components during normal operation. Helium is heated to 750°C in the core. The RPV directly connects to 100 cm of concrete on all sides (not depicted in Fig. 1c). Table I lists the key parameters of the base-case HTGR design.

The reactor is designed to shut down safely and passively during any incident. During a DLOFC, we assume complete containment failure. Other designs rely on residual pressure maintained in the containment building. For example, Huning et al.^[3] indicate that such ruptures are less probable and might be classified as a “beyond design basis” incident, and they assume an equilibrium pressure in the containment of 1.0 MPa. Heat transport by natural convection is negligible if the pressure drops to 0.1 MPa (e.g., Refs. [3] and [20]). Therefore, the reactor is designed at a low power density of 1.86 MW/m³ (compare, e.g., GT-MHR's 6.6 MW/m³). This also allows for horizontal installation, where buoyancy cannot drive the natural convection. No reactor cavity cooling system (RCCS) was adopted. Instead, the concrete outer boundary is fixed at environment temperature and forms the only heat sink of the system. For the power generation circuit, a simplified Brayton cycle was modeled.

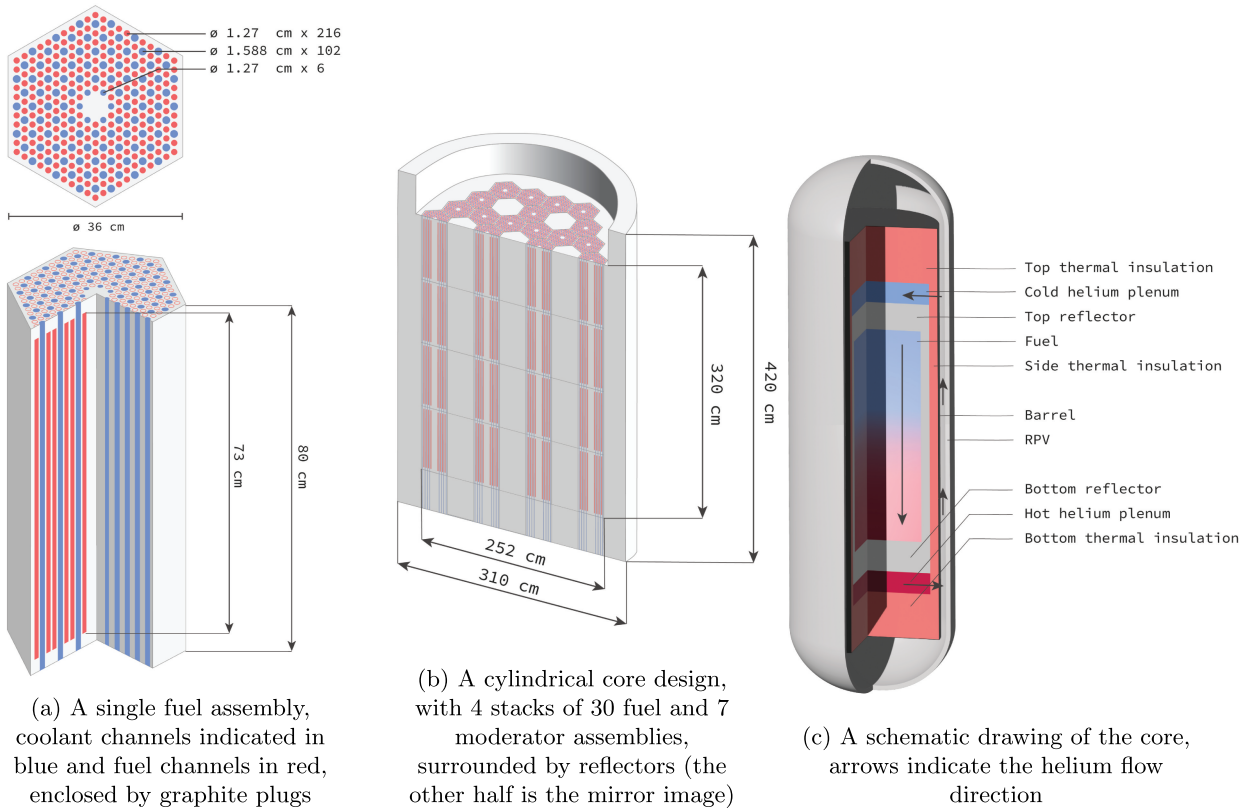


Fig. 1. Three schematic drawings showing the full core’s components at different levels.

TABLE I
Key Parameters of the HTGR Design

Reactor Type	Block-Type HTGR
Thermal power, P_{th} Power density, P''' Coolant gas	20 MW(thermal) 1.86 MW/m ³ Helium
Coolant channel inlet temperature, T_{in} Coolant channel outlet temperature, T_{out} Coolant channel pressure, P Total coolant mass flux, ϕ_m Coolant channel heat transfer coefficient, γ Graphite heat capacity, $c_{p,graphite}$ Graphite thermal conductivity, $\lambda_{graphite}$ Fuel thermal conductivity, λ_{fuel} SiC fiber insulation thermal conductivity, λ_{SiC} Steel thermal conductivity, λ_{steel} Concrete thermal conductivity, $\lambda_{concrete}$	250°C 750°C 4.0 MPa 7.64 kg/s 0.03 W/cm ² /°C 0.72 J/g/°C 0.036 to 1.31 W/cm/°C 0.014 to 0.19 W/cm/°C 0.065 W/cm/°C 0.55 W/cm/°C 0.013 W/cm/K
Fuel enrichment, η TRISO packing fraction, PF TRISO particle radius, r_{part} Fuel kernel (UO ₂) radius, r_{kernel} Graphite moderator density, ρ	20 wt% 0.3 510 μm 300 μm 2.0 g/cm ³

III. COUPLED CODE SYSTEM

III.A. Serpent

The homogenized macroscopic group cross sections are generated using the continuous-energy Monte Carlo code Serpent 2.^[15] We modeled the geometry exactly, including the randomly distributed TRISO particles. We made use of the symmetry, combining the information into five unique cross-section sets per layer. We also used Serpent to compute the microscopic ^{135}Xe cross section and the ^{135}I and ^{135}Xe fission yields.

The cross sections were homogenized per fuel assembly and were generated at three homogeneous core temperatures (21°C, 527°C, and 2227°C). The impact of assuming homogeneous core temperatures was estimated with Serpent and leads to ~ 10 pcm errors (using seven energy groups). The impact of using whole fuel assembly homogenization was tested axially and leads to ~ 20 pcm errors. Discontinuity and superhomogenization factors were not included; however, the impact is expected to be small because of the relatively small variations in cross sections compared to light water reactors.

The cross sections were erroneously computed using the 527°C thermal scattering $S(\alpha, \beta)$ library at each of the temperatures. The graphite thermal scattering cross sections increase significantly with temperature. Since the reactor is undermoderated, the temperature coefficient of reactivity is underestimated by between 15% (21°C to 527°C) to 25% (527°C to 2227°C). This is conservative for all of the modeled transients.

Our objective is to design an HTGR to operate for more than 20 years without refueling. The reactivity swing over time can be lowered from 35% to approximately 4% (e.g., Ref. [21]) by using fixed burnable poisons or thorium compacts, reducing the required reactivity of the control rods. We uniformly doped the TRISO fuel kernels with ^{10}B ($3.5 \times 10^{17}/\text{cm}^3$) throughout the core to reach $k_{eff} = 1$ at a uniform core temperature of 527°C at beginning of lifetime. Since control rod reactivity is an order of magnitude smaller than ^{10}B doping reactivity and we aimed at simulating incidents without control rod movement, the control rods were not explicitly modeled. For the preliminary burnup calculations, the core was kept at a uniform temperature of 527°C, but the sensitivity of the burnup to temperature variations was assessed and is included in the results.

During burnup calculations, each fuel assembly formed a depletion zone where the isotope inventory was tracked. More accurate burnup calculations require accounting for multiple depletion zones per fuel or poison pin. The

necessary working memory for such calculations was limiting; this can be solved by taking a multistep approach (e.g., first performing burnup calculations for representative single pins separately and later using the isotope inventory for these pins in whole-core calculations). This was deemed out of scope for this paper. In-assembly changes with burnup will therefore not be accurately computed.

III.B. PHANTOM-S_N

For the coupled simulations, we used the in-house code PHANTOM-S_N (e.g., Ref. [14]) to solve the Boltzmann neutron transport equation. PHANTOM-S_N is a discrete ordinates method code that solves the multi-group neutron transport problem on unstructured meshes. We used Gmsh^[22] to generate the meshes. The discontinuous Galerkin Finite Element Method is used in space, which is locally conservative and higher-order accurate. PHANTOM-S_N can determine k_{eff} , flux density, and power density distributions in both steady state and transients. PHANTOM-S_N includes code to determine the decay heat generation and ^{135}I and ^{135}Xe concentrations (^{149}Sm is not included).

The macroscopic group cross sections were homogenized over each fuel assembly. Linear interpolation was used to estimate the cross sections as a function of temperature. Six precursor groups were used to calculate the delayed neutron behavior, and standard decay heat data are used.^[23] The accuracy of spatial homogenization and fuel-moderator ratio is limited in two spots. First, six fuel rods are missing in the block-center for the assembly handling hole, which was not explicitly modeled. Second, we did not explicitly model the graphite plugs keeping the fuel rods in place at the top and bottom of each assembly (2×3 cm).

We verified the two-level Serpent–PHANTOM-S_N approach through a series of convergence analyses. First, it was confirmed that ordinate order S_2 and scatter order $N_S = 1$ were sufficient for modeling the reactor accurately. For the cylindrical layout where all 37×4 blocks are fuel assemblies, the effects on k_{eff} were limited when increasing the ordinate order to S_4 (+5 pcm) or increasing the scatter order $N_S = 2$ (−15 pcm). Note that 50-cm-thick graphite reflectors separate the upper and lower void plena from the core, lowering the impact on the angular distribution of the flux. These results confirm the diffusive character of the system. To speed up calculations in the future, the accuracy of a diffusion code could be researched, allowing for finer energy and spatial grids.

Second, the accuracy of PHANTOM-S_N in modeling current design (Fig. 1b) is analyzed. The power density peaks at the fuel-moderator boundaries because of the thermalized spectrum of neutrons. Figure 2 shows the power density from the middle of the core outward ($x = 0 \dots 160$ cm, $y = 0$ cm), in the middle of the third layer from the bottom ($z = 200$ cm) of the fuel assemblies. The results of Serpent and two meshes in PHANTOM-S_N are compared. We normalized the results for the total power in that plane to focus on radial effects only. The figure shows that with sufficient refinement, PHANTOM-S_N can calculate pin-level power density with $< 1\%$ error margins. The largest errors occur in the center of the fuel assembly since the missing fuel rods (i.e., increased moderator-to-fuel ratio and thermalization) there are not modeled by PHANTOM-S_N.

Next, the accuracy of PHANTOM-S_N for whole-core simulations is checked with a series of mesh refinement analyses. In the base case, a mesh comprising 5600 prismatic elements and an energy grid with seven groups was used, leading PHANTOM-S_N to calculate k_{eff} that was 840 pcm higher than Serpent. The mesh was refined radially (number of elements in r) and axially (number of layers in z), and the number of energy groups was increased from 7 to 17 and decreased from 7 to 3. Table II lists the error in the calculated k_{eff} , peak power density P'''_{max} , and the L₂ norm error of $P(x)$ (at $y = 0$ cm, $z = 200$ cm) and $P(z)$ (at $x = 33$ cm, $y = 0$ cm) compared to Serpent. Since the

graphite plugs (2×3 cm per fuel block) were not included in the PHANTOM-S_N model, to make the results comparable, only for this Table II did we run Serpent without graphite plugs as well.

Refining the energy grid is effective in reducing the error in k_{eff} but does not lower the error in P'''_{max} . Refining the mesh radially lowers the error in k_{eff} and P'''_{max} but is expensive. When both the energy grid and the spatial mesh are refined, k_{eff} is determined with an error of 69 pcm and a 2.2% error in P'''_{max} . If tests with a diffusion code prove successful, such fine spatial and energy grids could be used, possibly including the graphite in the middle of the fuel assemblies to get $< 1\%$ errors in the power density.

We chose the mesh that was four times refined in r and with eight extra layers in z , with 35 thousand elements. The peak power density is underestimated by 5.5%, mainly because of the axial homogenization of the graphite plugs. Figure 3 shows the mesh. For steady-state calculations, we chose the energy grid with seven groups (from Ref. [24]). The accuracy of the chosen settings for different uniform core temperatures is shown in Table III, which shows that k_{eff} is consistently overestimated by PHANTOM-S_N by around 675 pcm.

To speed up transient calculations, a three-energy-group structure (CASMO three-group structure) was used; this structure was developed for water reactors, and more research could yield a three-group energy grid giving more accurate results for the HTGR. However, Table II shows that while the error in k_{eff} is further off, the L₂ norm errors in $P(x)$ and $P(z)$ remain comparable to the finer energy grid. The grid boundaries of the seven- and three-group energy structure are listed in Table IV.

Note that the absolute error in k_{eff} between Serpent and PHANTOM-S_N is of secondary importance to the difference in the errors. While any absolute error during steady-state calculations can be compensated for by normalizing the fission neutron source, a relative error during transients may change the course of those transients. Table III shows that the relative errors are < 90 pcm for the different temperatures, leading to a 2% error in the temperature coefficient of reactivity. The standard deviations in the errors of a deterministic code are due to the stochastic errors in the homogenized group cross sections. These decrease with \sqrt{N} , where N is the total number of started neutron trajectories used by Serpent to compute the cross-section sets.

A second-order backward differentiation (BDF2) is used for temporal discretization in PHANTOM-S_N. We verified the time dependence for each component

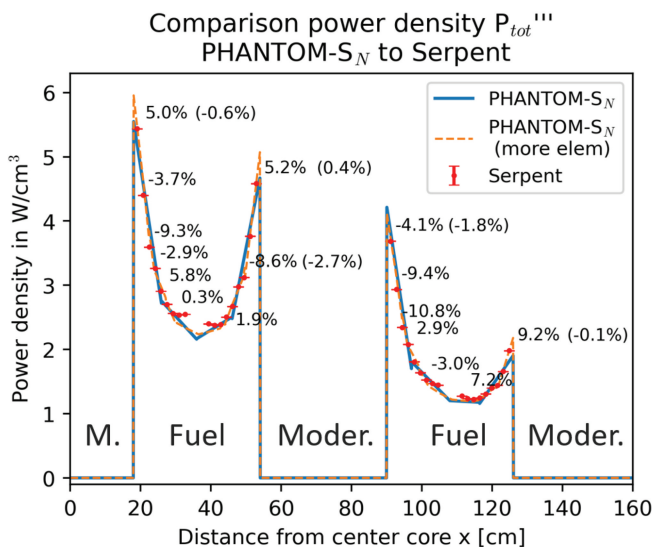


Fig. 2. A comparison of the total power density calculated by Serpent versus PHANTOM-S_N at the $z = 200$ cm plane, with alternating fuel and moderator blocks and only radial effects shown (axial effects are normalized out). The errors are indicated, and in parentheses are the errors when a finer mesh is used in PHANTOM-S_N.

TABLE II
Comparison of k_{eff} and P'''_{max} Found by Serpent and Difference with PHANTOM-S_N*

Case	Error k_{eff} [pcm]	Error P'''_{max} [%]	Error $\sqrt{\frac{\Delta P(x)^2}{P(x)^2}}$ [%]	Error $\sqrt{\frac{\Delta P(z)^2}{P(z)^2}}$ [%]
Base	+840	-20.6	14.2	17.1
Finer energy grid (7→17)	+243	-20.6	14.2	17.1
Finer mesh r (×4)	+656	-4.4	5.0	3.8
Finer mesh r (×7.4) and coarser z (-8)	+656	-11.4	8.1	15.9
Finer mesh z (+8)	+819	-17.1	13.5	12.1
Finer mesh r (×4) and z (+8)	+675	+3.0	5.3	2.3
Finer mesh r (×4) and z (+8) and coarser energy grid (7→3)	+1027	-15.3	6.9	2.7
Finer mesh r (×16) and z (+8) and finer energy grid (7→17)	+69	+2.2	3.3	2.1

*The error due to graphite plugs is compensated for to illustrate convergence.

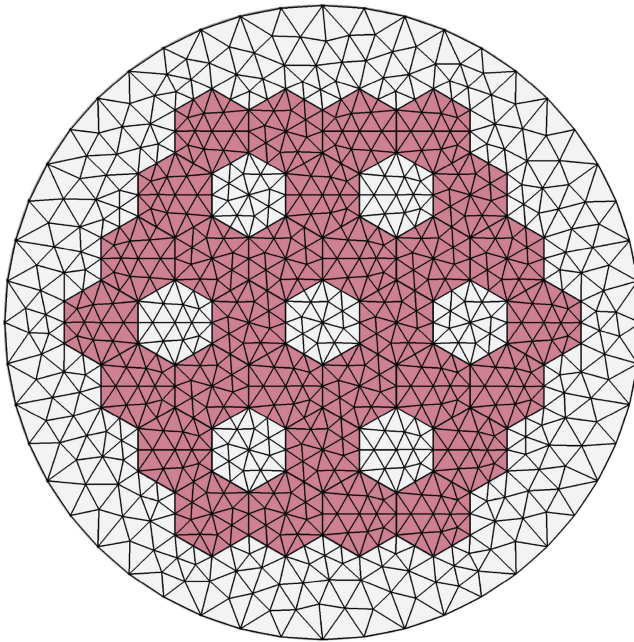


Fig. 3. Axial cut of the neutronics mesh used in PHANTOM-S_N.

(flux, delayed neutron precursor decay heat, xenon and iodine concentrations) separately. Second-order time convergence as well as convergence up to machine precision to theoretical solutions was verified.

III.C. Thermal Hydraulics

The temperature distribution of the nuclear system is calculated by the new in-house code OPERA. We used OPERA to calculate the temperature with four subcodes in four separate interdependent regions: (1) the solid core, (2) the RPV and concrete encasement, (3) the coolant in the core channels, and finally (4) the coolant throughout the power conversion system outside of the core. The interdependent system is solved iteratively. This section will introduce each subcode and includes a subsection to discuss the thermal conductivity of graphite.

III.C.1. Core

The temperature distribution in the core is calculated by solving the 3D time-dependent heat diffusion equation

TABLE III

Comparison of k_{eff} Found by Serpent and Difference with Phantom-S_N for the Seven-Group and Three-Group Cross-Section Sets

Case	Serpent	Δ PHANTOM-S _N
527°C (seven groups)	1.00014 ± 2 pcm	+675 ± 2 pcm
2227°C (seven groups)	0.95597 ± 2 pcm	+671 ± 2 pcm
527°C (three groups)	1.00014 ± 2 pcm	+1027 ± 2 pcm
2227°C (three groups)	0.95597 ± 2 pcm	+1116 ± 2 pcm

TABLE IV
The Seven Groups for Steady State
and Three Groups for Transients*

Seven Groups	Three Groups
6.74E+04	8.21E+05
7.49E+02	6.25E-01
1.59E+01	
1.93E+00	
3.50E-01	
3.00E-02	

*Energy grid boundaries are in units of electron volts.

$$\rho c_p \frac{\partial T(\vec{r}, t)}{\partial t} = \nabla \cdot \lambda(T, T_{irrad}) \nabla T(\vec{r}, t) + q'''(\vec{r}, t) \quad (1)$$

The core temperature T is determined on the power density $q'''(\vec{r}, t)$ at point \vec{r} and time t . The isotropic thermal conductivity λ depends on the temperature T and the irradiation temperature T_{irrad} . Furthermore, the heat capacity $c_{p,gr}$ and density ρ influence transient behavior. Table I lists the values of these parameters.

In the current model, the heat capacity is kept constant at cold conditions, while in reality it increases with temperature by more than 100%. All increasing temperatures during transients are therefore overestimated. Moreover, the heat transfer coefficient of the coolant channel is currently kept constant, while it approximately linearly increases with the coolant channel mass flux. It is set to the value corresponding to a total mass flux for the 20-MW(thermal) design. Therefore, it is underestimated by $\sim 50\%$ for the 40-MW(thermal) design, causing overestimated temperatures in the core.

OPERA solves Eq. (1) using the symmetric interior penalty Galerkin (SIPG) approach.^[25] A thermal radiation boundary condition was imposed between the reactor core sides and the RPV. Owing to the thick neutron reflector inhibiting heat flux from the core to the upper and lower plena, we assumed an insulating boundary condition at the top and bottom of the reactor. All power was deposited in the fuel pins. These are both conservative estimations increasing the maximum temperature.

We verified OPERA by comparing to analytical solutions, confirming the higher-order convergence of the SIPG method and convergence up to machine precision. Each boundary condition, as well as each module of OPERA, was verified in a similar way. The mesh was chosen after a series of mesh convergence studies. We

chose a mesh with 2.6 million second-order prismatic elements and first-order basis functions. A BDF2 temporal discretization was used, and convergence was verified in a similar way as PHANTOM-S_N. The maximum temperature error is 1°C. Figure 4 shows an excerpt of the mesh at the side of a fuel assembly.

The model is simplified in two ways. First, we assumed perfect conduction everywhere in the core: between blocks, between fuel pellets themselves, and between fuel pellets and graphite blocks. In steady state, little effect is expected from the block-to-block conduction assumption because of symmetry. During transients, uncertainty may increase. From Ref. [26], we estimate the pellet-block conduction assumption to lead to a maximum 20°C underestimation of fuel temperature for our parameters. Second, individual TRISO particles are homogenized, leading to a 2°C underestimation of the maximum temperature in steady state. The underestimate is approximately proportional to the maximum power density. During a reactivity insertion transient, the underestimate may therefore grow. Delays in transporting heat from the kernel to compact do not play a role; the characteristic timescale of heat transport (at distances around TRISO particle size, around 500 μm) is over two orders of magnitude smaller than the timescales of the reactivity power surges.

III.C.2. Heat Conductivity Model

Irradiation damage can degrade the heat conductivity of nuclear graphite by more than an order of magnitude. The temperature during irradiation (called irradiation temperature) T_{irrad} is the most important factor, followed by the fluence and the temperature during measurement (called temperature) of the thermal conductivity. To our

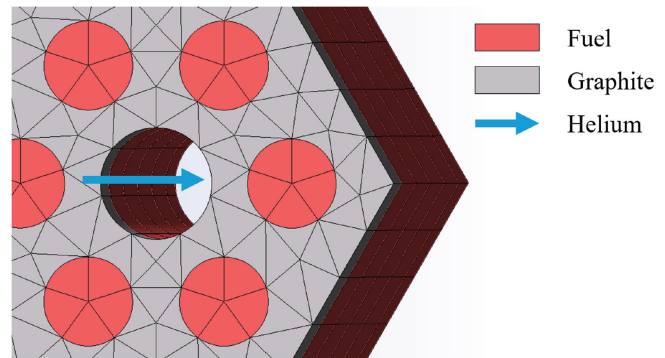


Fig. 4. An excerpt of the thermal-hydraulic mesh showing the corner of a single fuel assembly.

knowledge, most other models neglect the effect of irradiation temperature. Some use a fixed value (e.g., Refs. [27] and [28]). Others use temperature to model pebble-to-pebble radiation (but not for the graphite itself), like, for example, the Pronghorn code system^[29]; Ref. [30] (using TINTe) and Ref. [31] (using THERMIX) consider the radiation temperature and dose. We found only one code that includes a model for the thermal conductivity as a function of irradiation temperature, measurement temperature, and fast fluence, which is VSOP's (version 11/05) THERMIX.^[13] However, publications using THERMIX either do not report on the used model for the thermal conductivity or use models that include only dose or measurement temperature. To our knowledge, there is no other HTGR code that combines these three parameters, nor any publication using the three parameters in HTGR incident modeling and reporting on it.

The dominant mechanism that limits thermal conductivity is phonon scattering. In unirradiated graphite above room temperature, phonon-phonon scattering prevails. An increase in temperature increases the chance of scattering, lowering the conductivity. However, irradiation causes the conductivity to decrease as a result of two other effects. First, the conductivity decreases rapidly at the crystal level because of irradiation-induced lattice defects that form phonon-scattering points. The defects are mobile and recombine at a temperature-dependent rate. These competing processes reach an equilibrium conductivity (at saturation dose) that decreases strongly with decreasing temperature. This saturation level depends only on the irradiation temperature and not on the material or orientation.^[12] Second, the thermal conductivity decreases from equilibrium as a result of porosity generation at higher fluences (called the break-away dose). This superimposed structural change starts at doses that decrease with increasing temperature.

We developed a simplified model that includes the irradiation temperature and the current temperature. This model uses the relation proposed by Kelly^[32] that the thermal resistances can be superimposed:

$$\frac{1}{\lambda} = \frac{1}{\lambda_0} + \frac{1}{\lambda_D} \quad , \quad (2)$$

where λ = total thermal conductivity; $1/\lambda_0$ = resistance in unirradiated graphite; $1/\lambda_D$ = resistance due to irradiation-induced lattice defects. Most documented experimental results relating thermal conductivity, irradiation temperature, and dose were measured at room

temperature. However, for our simulations, we need the thermal conductivity at reactor temperature. Haag^[12] proposes Eq. (3) to relate these:

$$\frac{1}{\lambda(T, T_{irrad})} = \frac{1}{\lambda_0(T)} + \frac{1}{\lambda_0(T_{RT})} \cdot \left(\frac{\lambda_0(T_{RT})}{\lambda(T_{RT}, T_{irrad})} - 1 \right) . \quad (3)$$

Here, we have introduced measurement (or current reactor) temperature T and irradiation (over a period of time) temperature T_{irrad} . We assumed after Haag^[33] that the irradiation-induced thermal resistance $1/\lambda_D$ is independent of the measurement temperature.

The model was simplified by including only the saturation level thermal resistance. The THERMIX code includes an estimate of the break-away dose [γ_{BA} in/cm² (EDN)] and saturation dose [γ_{SAT} in/cm² (EDN)]—EDN is the equivalent fluence in the former DIDO reactor^[34]—with

$$\gamma_{BA} = (a \cdot T_{irrad} + b)$$

$$\gamma_{SAT} = \gamma_{BA}/c \quad ,$$

where T_{irrad} is in degrees Celsius; $a = -0.1082 \times 10^{20}$ /cm² (EDN)/K; $b = 179.17 \times 10^{20}$ /cm² (EDN); $c = 3$. The saturation level dose is first reached after 5 years in the center-bottom of the reactor core being designed here and last reached after 15 years at the side-top of the reactor. The break-away dose is reached after approximately 19 years at the center-bottom of the active core.

A function was developed by fitting data from graphite irradiated at temperatures from 295°C to 1410°C (from the Nuclear Graphite Knowledge Bank^[35]). The change in thermal conductivity as a function of irradiation temperature, measured at room temperature, is sought after, and a simple polynomial of the form

$$\frac{\lambda(27.5, T_{irrad})}{\lambda_0(27.5)} - 1 \approx d \cdot T_{irrad}^2 + e \cdot T_{irrad} + f \quad , \quad (4)$$

with T_{irrad} in degrees Celsius, $d = -1.215 \times 10^{-7}/K^2$, $e = -5.379 \times 10^{-4}/K$, and $f = -1.120$, resulted in a fit with $R^2 = 93\%$. The experimental data and the fit are shown in Fig. 5. The increase in thermal resistance can be found by rewriting Eq. (4) and fitting the data with $R^2 = 86\%$. Since TRISO fuel compacts consist of over 80% graphite, the same irradiation damage relations were applied to these materials as well.

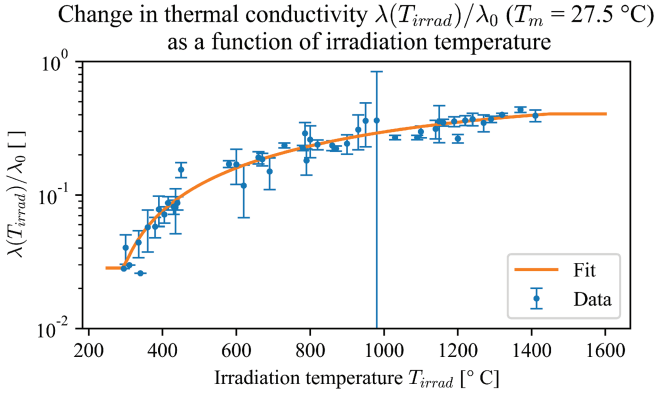


Fig. 5. Fit of thermal conductivity as a function of irradiation temperature measured at room temperature, divided by the thermal conductivity of unirradiated graphite measured at room temperature.

For the unirradiated graphite, the relation

$$\lambda_0(T) = g \cdot T^2 + h \cdot T + i \quad (5)$$

was used from Ref. [36], with T in degrees Celsius, $g = 3.719 \times 10^{-7} \text{ W/cm/K}^3$, $h = -1.074 \times 10^{-3} \text{ W/cm/K}^2$, and $i = 1.340 \text{ W/cm/K}$ for the matrix graphite. For the TRISO compacts, the effective thermal conductivity was determined using relations for distributed spheres in a homogeneous material. The model was developed by Chiew and Glandt,^[37] and we used the fitting parameters proposed by Ref. [38] including the effective thermal conductivity of a single TRISO particle from Ref. [39] ($4.13 \times 10^{-2} \text{ W/cm} \cdot \text{K}$). The model finally yields $g = 1.193 \times 10^{-7} \text{ W/cm/K}^3$, $h = -3.446 \times 10^{-4} \text{ W/cm/K}^2$, and $i = 0.43 \text{ W/cm/K}$.

The model includes four approximations. First, we used the saturation level thermal resistance in combination with fresh fuel cross-section libraries. With fresh fuel, the power density peaks at the inner fuel-moderator assembly boundaries, yet it will have flattened radially before the saturation fluence is reached. The combination of saturation thermal conductivity and fresh fuel will overestimate the fuel temperatures especially at graphite-fuel assembly boundaries. Second, diffusivity recovery was not considered. The increased temperature during incidents can restore the graphite. It has been shown that for annealing at 1600°C for 43 h, the conductivity is completely recovered.^[40] Third, we used the heat capacity of 0.72 J/g/K , which holds at 45°C , while in reality it increases with temperature from 1.2 J/g/K (250°C) up to 1.9 J/g/K (1500°C). Fourth, the second breakdown of thermal conductivity at high fluences was not modeled. The first three limitations are conservative.

The fourth limitation is not. However, we estimate that the second increase of thermal conductivity at break-away fast fluence γ_{BA} starts after 19 effective full-power years (EFPY) at the cold top, only 1 year before end of life. The impact on the maximum temperature is estimated to be negligible.

III.C.3. RPV Model

The RPV is separated from the active core by the neutron reflector, thermal insulation, the barrel, and the gas gap. Figure 6 graphically represents the geometry and the mesh connection. We assumed that thermal radiation is the sole mode of heat transfer to the RPV and that helium conductivity does not play a role. Since the RPV is relatively well insulated from the fuel, we simplified the code by modeling the RPV as a set of N one-dimensional (1D) equations in radial dimension, where N is the number of barrel surface elements. Each barrel element connects to a single RPV boundary element, and every

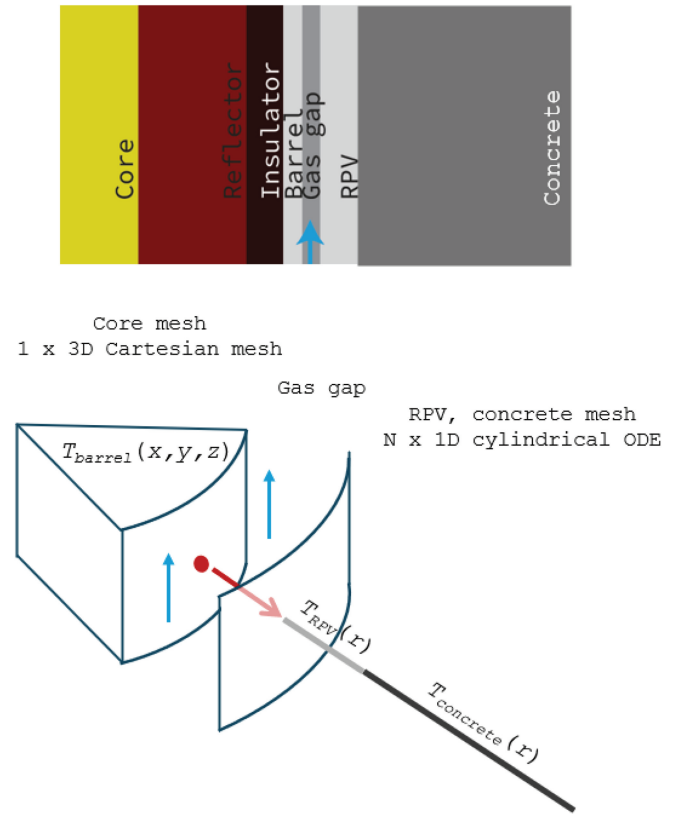


Fig. 6. Top: A 2D representation of the core and surrounding structures. Bottom: Approach in modeling the thermal radiation boundary, with the core, reflector, insulator, and barrel modeled in three dimensions and the RPV, concrete in N 1D ordinary differential equations (ODE).

single 1D equation is uncoupled from all others. This is schematically drawn in Fig. 6.

The temperature in the RPV $T(r)$ can then be determined with Eq. (1) in cylindrical coordinates by including the heat flux at the boundary,

$$q''_{2 \rightarrow 1} = \frac{\sigma_{SB}}{v_{21}} (T_2^4 - T_1^4) \quad , \quad (6)$$

where

$$v_{21} = \frac{S_1}{S_2} \frac{1 - \varepsilon_2}{\varepsilon_2} + \frac{S_1}{S_2 F_{21}} + \frac{1 - \varepsilon_1}{\varepsilon_1} \quad . \quad (7)$$

Radiative heat transfer $q''_{2 \rightarrow 1}$ is the surface power density from surface 2 to surface 1. If surface 2 is the RPV and surface 1 is the core, then $q''_{2 \rightarrow 1}$ is generally negative. It is calculated with the Stefan-Boltzmann constant σ_{SB} , the RPV boundary temperature T_2 , and core boundary temperature T_1 . The surface center temperature is used. The dimensionless parameter v_{21} is determined based on the ratio of the element surface areas S_1 (core) and S_2 (RPV) and the view factor F_{21} . For the RPV boundary condition, we use $q''_{1 \rightarrow 2} = -\frac{S_2}{S_1} q''_{2 \rightarrow 1}$. The equation is solved by the SIPG method,^[25] and temporal discretization is done by BDF2.

This method introduces three simplifications. First, using the one-dimensional equations implies that heat conductivity in tangential and axial dimensions in the RPV and surrounding concrete is neglected. The thermal resistivity of the side neutron reflector, thermal insulation, and barrel will have flattened the axial and tangential temperature dependence, so that the simplification will have small effects on core cooling during incidents. Second, each core element radiates heat only to a single RPV element, or $F_{12} = \frac{S_2}{S_1} F_{21}$ for each connection. Since the heat conduction is constrained to the radial direction only, the RPV temperature will be overestimated where the core temperature is highest, thereby lowering the overall radiative heat transport as core-side hot-spot thermal radiation cannot be transported to cooler RPV spots. These simplifications are therefore conservative for both the core and the RPV temperatures. Finally, helium thermal conduction is neglected, thereby further lowering heat transfer. This simplification is conservative for core temperature but not for RPV temperature.

III.C.4. Coolant

We calculated the helium temperature $T_{he}(z)$ in the coolant channels along z by solving

$$\phi_m c_{p,he} \frac{dT_{he}(z)}{dz} = \pi D \gamma (\langle T_{gr}(z) \rangle - T_{he}(z)) \quad (8)$$

per channel. Here, we introduced the coolant mass flux ϕ_m , specific heat capacity $c_{p,he}$, channel diameter D , and heat transfer coefficient at the channel wall γ . Since helium flow is turbulent (the Reynolds number lies between 4.0×10^3 and 6.5×10^3) during normal operation, we assumed that there is only z dependence of temperature. Therefore, we used the average temperature along the channel's circumference to calculate the heat flux. We solved Eq. (8) by the discontinuous Galerkin approach with first-order basis and test functions. The relevant parameters are listed in Table I. The upper and lower plena were not modeled.

The pressure drop along the channels is relatively small (around 100 Pa) compared to the steady-state system pressure, justifying our assumption that the pressure is constant in time and space. However, the combination of constant pressure, incompressibility, and an ideal gas cause the temperature dependence on time to be zero. Noting that the ideal gas equation of state reads $\rho(P, h) = \zeta / (\zeta - 1) \frac{P}{h}$, where h is the enthalpy and ζ is the specific heat ratio, and noting that $T(h) = c_p^{-1} h$, we find that

$$\rho_{he} c_{p,he} \frac{dT_{he}}{dt} = \zeta / (\zeta - 1) \frac{dP}{dt} = 0 \quad . \quad (9)$$

The thermal capacity of the helium during transients is therefore not taken into account. This is a conservative assumption.

The two most important limitations are the following. First, bypass flow between the prismatic assemblies was not modeled. Bypass flow causes extra cooling between the prismatic blocks, which causes the block's center temperature to rise. For instance, Tung et al.^[41] calculated a 73°C increase of T_{max} . Tak et al.^[26] calculated a maximum increase of 79°C. However, both studies modeled 1/12th of a fuel assembly in an infinite lattice, which does not include a peak in power density at reflector-fuel assembly boundaries. Depending on the fuel distribution, a bypass gap might lower the maximum temperature if it is reached close to the gap. Second, the coolant temperature is assumed to be well mixed. The radial temperature difference reported in literature varies: Tung et al.^[41] report a difference of approximately 30°C (pressure of 64 bars, mass flux of 23 g/s, channel wall heat flux of 12.3 W/cm²) while Tak et al.^[26] show a temperature difference of approximately 100°C over

the channel (69 bars, 23 g/s, 13.6 W/cm²). Since our reactor has a smaller heat flux over the coolant channel boundary ($q''_{max} = 7.4$ W/cm²), we estimate the radial difference between the average and maximum temperatures to be 25°C. The coolant temperature at the wall and the fuel temperature may thus be underestimated by 25°C.

III.C.5. Intermediate Heat Exchanger

The coolant inlet temperature T_{inlet} can change during transients. This may happen when, for example, the reactor power increases during a reactivity insertion incident or if the mass flux decreases as a result of a partial blockage. The change in T_{inlet} depends on the power conversion system. We estimated T_{inlet} as a function of time by modeling a simplified power conversion system comprising two loops and external cooling.

Figure 7 shows how the primary and secondary circuits were connected by heat exchanger AB. We modeled a Brayton cycle with isobaric and adiabatic legs. We included heat transfer at the heat exchangers between loops and at the core. All fluid parameters except temperature were kept constant. We omitted the power conversion system, which would otherwise include turbines, compressors, and possibly intercooling or reheating stages. We modeled counterflow heat exchangers. The primary circuit's helium is cooled from T_0^A to T_L^A while heating the secondary's circuit working fluid from T_L^B to T_0^B . The secondary circuit rejects its heat at heat exchanger CD, cooling its fluid from T_0^C to T_L^C and heating the environmental cooling fluid from T_L^D to T_0^D . No latent heat was modeled, corresponding to a Brayton cycle.

The temperature derivative $\frac{dT^A(x)}{dx}$ along the flow direction x on side A in a heat exchanger is

$$\frac{dT^A(x)}{dx} = \frac{h_{tot}\pi D}{\phi_m^A c_p^A} (T^A(x) - T^B(x)) \quad , \quad (10)$$

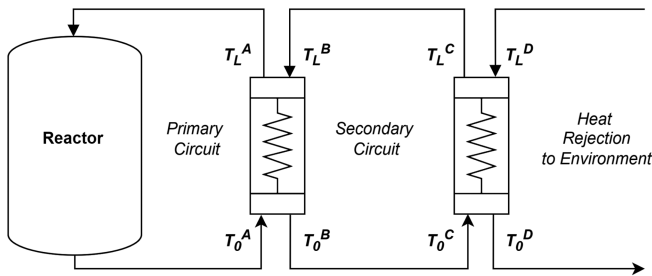


Fig. 7. Schematic drawing of the primary and secondary loops, including heat exchangers AB and CD.

with tube diameter D and height h_{tot} . Including the temperature derivative on side B and the overall heat balance, the total heat flux ϕ_q^{AB} over heat exchanger AB can be found as

$$\phi_q^{AB} = \gamma_{tot}^{AB} \cdot A^{AB} \cdot \frac{(T_L^A - T_L^B) - (T_0^A - T_0^B)}{\ln((T_L^A - T_L^B)/(T_0^A - T_0^B))} \quad , \quad (11)$$

where γ_{tot}^{AB} = total combined heat transfer coefficient, including convective and conductive heat transfer of the heat exchanger material; A^{AB} = total heat-exchanging surface area. Heat flux ϕ_q^{CD} can be found in the same way.

For maximum efficiency, the ratio of the temperature at which energy is received to the temperature at which energy is rejected must be maximized. We modeled heat exchangers with high effectiveness $\eta_{HX} = 95\%$, which is the ratio of actual heat transfer to the maximum possible heat transfer, or

$$\eta_{HX-AB} = \frac{T_0^B - T_L^B}{T_0^A - T_L^A} \quad . \quad (12)$$

The size of the heat exchanger grows exponentially as η_{HX} increases asymptotically to 100%.

During transients, we assumed a 2-s delay in each leg. The accuracy of the model is limited by several simplifications. First, quasi-steady-state equations are used in the heat exchangers. We furthermore omitted modeling turbines and compressors. Time dependence is included only by assuming a delay in the hot and cold ducts. The thermal capacity of the gaseous and solid materials of the heat exchanger is neglected, as are those of the turbines and compressors. The simplifications entail that the heat exchanger outlet temperature (and thus core inlet temperature) responds more quickly to the core outlet temperature variations. To study the sensitivity of the core temperature to the secondary system, we varied leg delay times. Section V.F details the results.

IV. COUPLED SIMULATION METHODOLOGY

The coupling strategy used is shown in Fig. 8. PHANTOM-S_N uses the flux to determine the power density, which is passed to OPERA at the fuel pin numerical integration points (by Gaussian quadrature). All fission and decay heat power is assigned to the fuel pins, while in reality only 80% of the power is deposited

locally by fission fragments. The increased ($\sim 25\%$) fuel power density is conservative, and it more than makes up for the 2×3 -cm graphite plugs, which were not modeled explicitly in OPERA ($\sim 7.5\%$ lowered power density). The fuel rods were modeled as extending over the entire 80-cm fuel blocks instead. OPERA computes the fuel temperature at subpin precision.

For fuel assemblies, OPERA passes the average fuel temperature per block B to PHANTOM-S_N. In reality, the fuel and the graphite temperatures each have a distinct effect on the core reactivity, both in terms of delay and strength. The fuel temperature coefficient of reactivity is somewhat larger (a factor 1.5 to 2; see Ref. [16]) than the moderator coefficient. The moderator coefficient is more delayed—the timescale of conductivity to the moderator is ~ 10 s. We chose to use only the fuel temperature (in fuel assemblies) to interpolate the cross sections since that feedback effect is strongest and will yield the most accurate results. However, it is not conservative since the reactivity feedback rate is overestimated (< 10 s). For moderator assemblies, the average graphite temperature is used.

For steady-state calculations, the coupled code is iteratively run until $\Delta k/k$ (1 pcm) and temperature $\Delta T/T$ (0.1 K) between two iterations converge, as shown in Fig. 8. Note that k_{eff} will converge to approximately $1.0 + 675$ pcm (see Table III). A more natural strategy is to update the power iteratively until convergence of $k_{eff} = 1.0$. However, the error in k_{eff} as calculated by PHANTOM-S_N of around 675 pcm will cause a relatively large difference $T_{avg,f}$ ($\sim 150^\circ\text{C}$). Since maximum reactor temperature is the most important parameter for the safety calculations in this paper, we decided to allow the system to converge to $k_{eff} \neq 1$ while maintaining a fixed total power. During steady state, helium flow at the gas gap is not explicitly modeled. Instead, the barrel and RPV surface temperatures are fixed at the helium inlet temperature of 250°C .

For transient calculations, Fig. 8 shows how PHANTOM-S_N is run first to determine the power density distribution at the next time step t^i , after which OPERA is run. OPERA passes a linear estimate of $T(t^{i+1})^*$ to PHANTOM-S_N. A BDF2 is used in all codes. The coupled second-order time convergence was verified, as well as convergence up to machine precision to analytical solutions. Using four cores of an Intel(R) Xeon(R) CPU E5-2630 v2 processor at 2.60 GHz, finding a steady state takes approximately 34 h (seven coupled iterations). Calculating a time step costs PHANTOM-S_N ~ 700 s and OPERA ~ 3000 s.

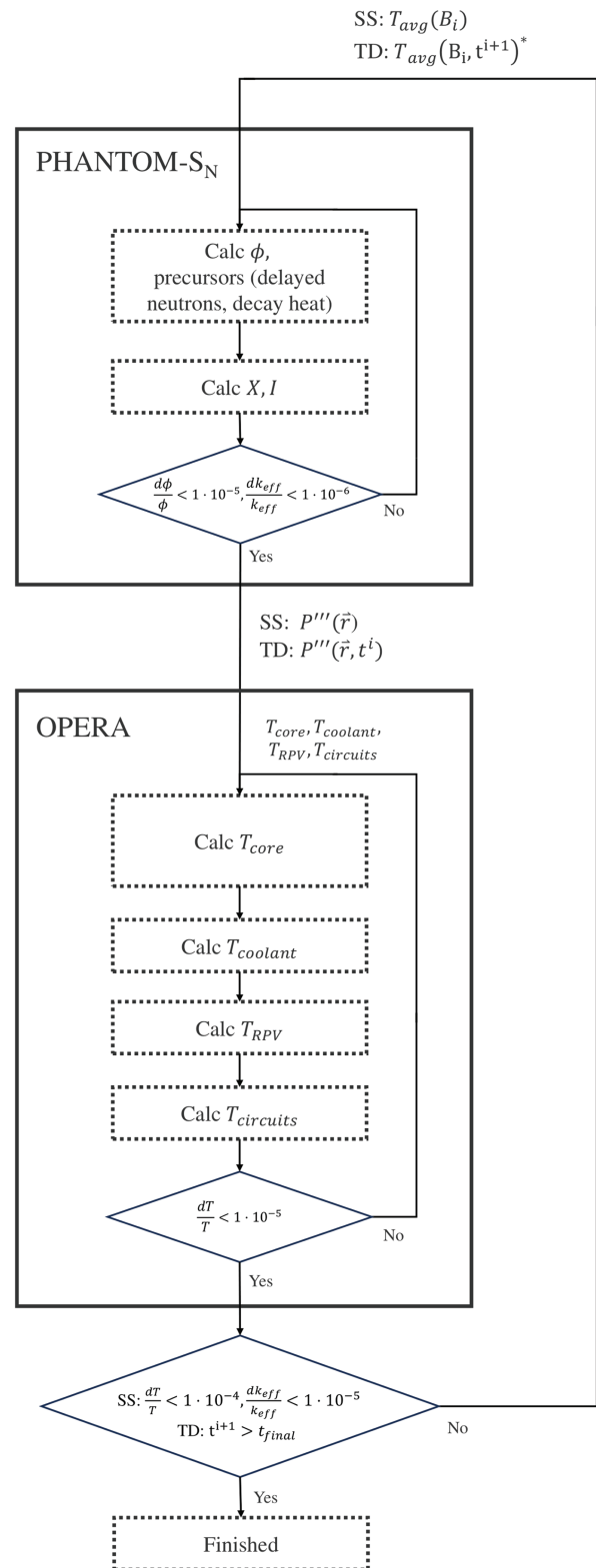


Fig. 8. Schematic diagram of the codes, including the inner iterations in PHANTOM-S_N for angular flux ϕ , ^{135}Xe X and ^{135}I I concentrations, and the inner iterations in OPERA for the temperature of all components; OPERA passes the block B_i average temperature to PHANTOM-S_N.

IV.A. Depressurized Loss of Forced Cooling

First, we modeled a DLOFC. During the DLOFC, we simulated a stop of the helium pumps and a pressure drop to 1 bar in the primary circuit. We assumed that natural convection does not play a role in heat transfer (e.g., Refs. [3] and [20]). The onset of the incident was simulated by setting the coolant channel heat transfer coefficient to 0 instantaneously. The fixed temperature boundary condition at the barrel and RPV was set to a thermal radiation condition. Since the DLOFC is generally seen as the severest incident, three different DLOFC events were run to investigate different possible reactor operation modes. First, we researched the 20-MW(thermal) base case, where helium was heated from 250°C to 750°C. Second, we examined the possibility of running the reactor at 40 MW(thermal): Steady-state power and coolant mass flux were doubled. Third, we tested a reactor at increased temperature. In this 20-MW (thermal) design, the mass flux was increased (factor of 1.3), and helium was heated from 520°C to 900°C after a HTGR power conversion system proposed in Ref. [18], which may reach 51.5% thermal efficiency.

IV.B. Partial Blockage

Second, we modeled a partial blockage. During a DLOFC, the fuel temperature increases throughout the entire core, causing strong reactivity feedback. If on the other hand, only a single channel is blocked, the fuel temperature will increase relatively little, but the flux will remain nearly unchanged. The maximum fuel temperature reached therefore depends on the number and combination of coolant channels blocked.

Therefore, despite the widely adopted fact that a DLOFC is the most severe incident, a partial blockage may be more so for TRISO fuel failure for the prismatic type of microreactor if it remains undetected. A DLOFC remains more severe for barrel and RPV temperatures exceeding the design limits. While the probability of such an event occurring may be smaller than a DLOFC, the International Atomic Energy Agency^[42] lists the incident “partial clogging of the fuel assembly flow area by a fuel assembly fragment” as a design-basis accident. Barsell et al.^[43] indicate that during thermal transients with temperatures exceeding 815°C in the upper plenum, the thermal barrier cover plate might come loose, leading to a partial blockage.

Moreover, a partial blockage event could be more difficult to detect than a DLOFC. Changes in coolant

flow or outlet temperature may be small, as well as the flux variations at neutron detectors surrounding the core. Therefore, a partial blockage may not only be the most severe incident due to limited thermal feedback but also where passive safety plays the most important role.

The partial blockage event was modeled by setting the heat transfer coefficient of specific groups of coolant channels to 0 instantaneously. We tested two blocked channel incidents, blocking all channels in one or three fuel assembly stacks. Figure 9 shows which single stack (solid line) or three stacks (dashed line) were blocked, chosen for their high power density.

During the DLOFC case, the power conversion cycle did not play a role since the coolant flow was set to 0 instantaneously after steady state. Here, the helium inlet temperature will change because of the change in total reactor power with continuing helium circulation.

IV.C. Reactivity Insertion and Water Ingress

Third, we modeled a reactivity insertion incident. The reactivity insertion may have been the result of an operator error or because of water ingress. Virtually all HTGRs being designed are strongly undermoderated such that water

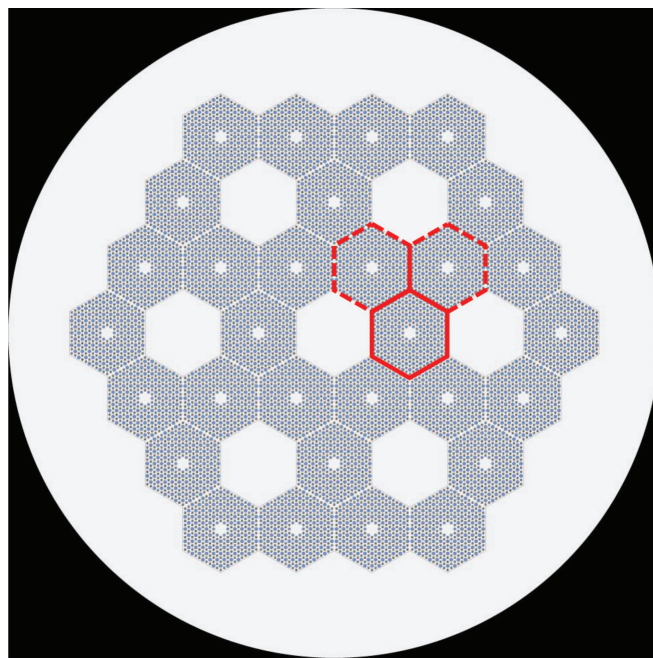


Fig. 9. Axial cut of the core, with the blocked stacks indicated with red solid (one stack) and dashed (three stacks) lines.

ingress may lead to a large reactivity increase. We tested the maximum allowable reactivity increase in a single-stack sensitivity study and a full-core simulation, and we tested the possible reactivity insertion as a function of coolant channel water density. While in reality there would be a gradual increase in reactivity, we conservatively modeled an instantaneous increase. This will cause the fuel temperature to further lag behind the increased fission power, delaying feedback and increasing the peak fuel temperature. Only the neutronics inputs were changed; the changes in coolant density were not changed. In reality, maximum reactivity is reached at a water density that is two orders of magnitude larger than that of helium. This will help cool the core by transporting heat to the heat exchangers, and neglecting this effect is conservative. The power conversion loop will play a role in

determining the reactor inlet temperature, as the heat exchangers are unable to transfer all extra power.

V. SIMULATION RESULTS

V.A. Steady State

The coupled code reached steady state after seven coupled iterations. Figure 10 shows the power and temperature distribution of the 20-MW(thermal) base case. Table V lists the results for four steady-state scenarios: the base case, a 40-MW(thermal) case, and a high helium temperature case (inlet 520°C and outlet 900°C), and a case where the thermal conductivity was fixed to the cold unirradiated value.

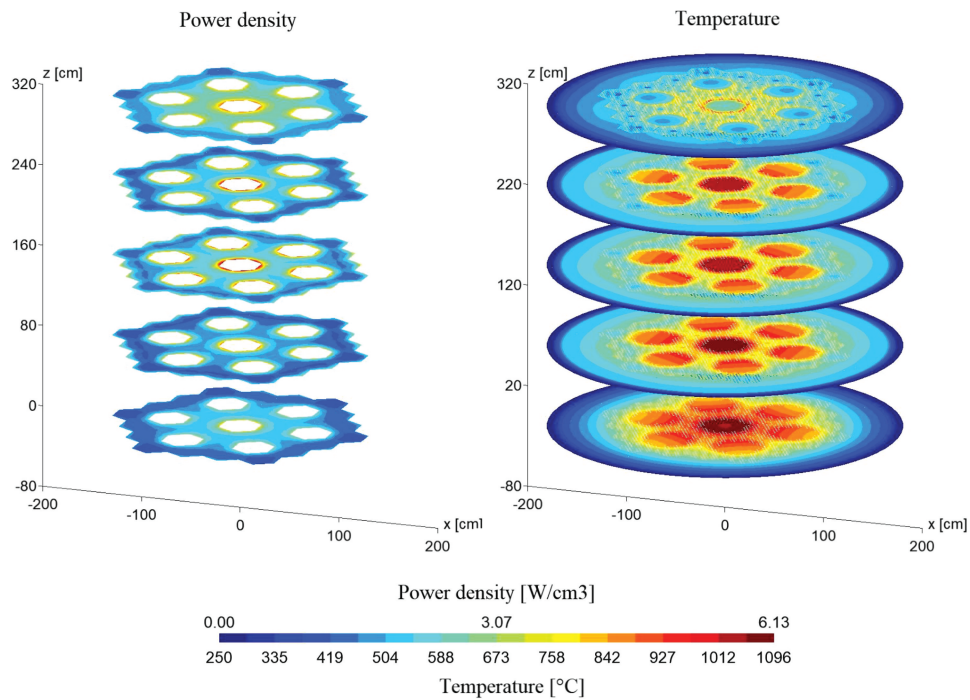


Fig. 10. Steady-state [20-MW(thermal)] power density (left) and temperature (right).

TABLE V

Steady State Results

Case	T_{max} (°C)	T_{avg} (°C)	$T_{avg,f}$ (°C)	P'''_{max} (W/cm ³)
20 MW(thermal)	1169	508	649	6.1
40 MW(thermal)	1420	593	784	12.2
20 MW(thermal), T^{900}	1276	735	851	6.1
20 MW(thermal), λ^{fixed}	1004	506	634	6.1

The power density peaks at every graphite-fuel interface because of the softened spectrum. The relatively large TRISO kernel radius (300 μm) and the high enrichment (20%) further increase these peaks, reaching a maximum of 3.2 times the average power of 1.9 W/cm³ around the central moderator block. Figure 11 shows the axial profile at three different locations along at y = 0 cm. The expected shape of a cosine about the center is visible, although the top and bottom reflectors cause another power peak at the axial reflector-fuel boundaries. The radial temperature varies up to 320°C (in the z = 60 cm plane) in a single fuel block as a result of the power density variations, and strong variations in the helium outlet temperature are found, which range from 545°C to 1027°C.

Figure 12 shows the temperature distribution at the top of the core (z = 320 cm) in the fuel assembly right of the central moderator block. The figure illustrates the importance of modeling the fuel pins and graphite explicitly. The cold helium at the top of the core causes the graphite thermal conductivity to deteriorate relatively strongly. The temperature difference between pin center and coolant channel boundary is 115°C. If the graphite and fuel were homogenized, the pin center temperature would drop to the average temperature, leading to an underestimation of approximately 80°C. Moreover, the thermal conductivity at the coolant channel wall would be overestimated by ~35%, causing a further error in the maximum temperature calculation.

For simplicity, ¹⁰B was distributed uniformly across all TRISO kernels in these simulations. However, choosing a

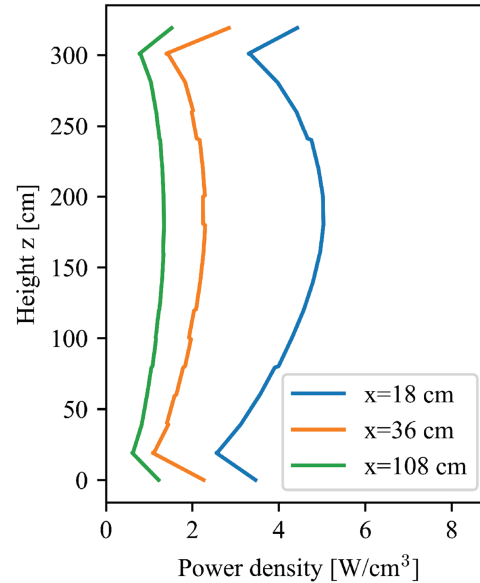


Fig. 11. Axial power profile at three locations in x and all at y = 0 cm.

¹⁰B distribution that flattens the power density would improve reactor safety. A lower maximum power density is especially important to prevent a local steep increase of maximum temperature during reactivity insertion incidents. Moreover, it would help against “hot-streaking.” Finally, the design could make better use of graphite as a thermal buffer. Figure 10 demonstrates how the moderator blocks are relatively hot. We estimate that with a ¹⁰B redistribution, the

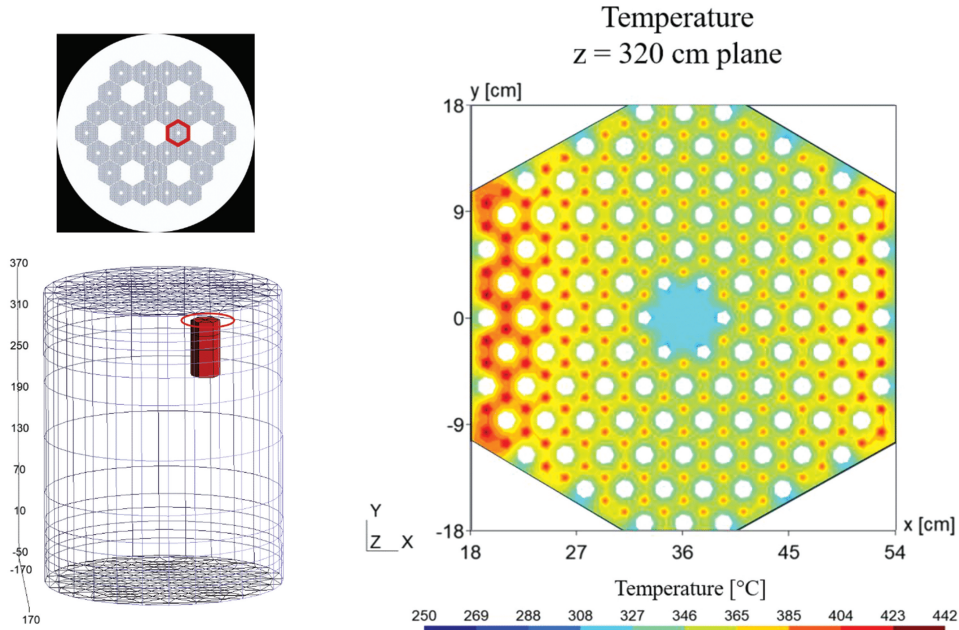


Fig. 12. Temperature distribution at the top of the core (z = 320 cm plane) just right of the central moderator block.

steady-state radial temperature differences could be lowered by more than 200°C

Finally, Table V shows the importance of including thermal conductivity as a function of irradiation temperature. The 20-MW(thermal) design was run with fixed (called λ_{fixed}) thermal conductivity values for unirradiated materials measured at room temperature (we used $\lambda_{graphite} = 1.31$ J/cm/K and $\lambda_{fuel} = 0.43$ J/cm/K). The code shows that the maximum fuel temperature would be underestimated by 165°C.

The steady-state temperature is overestimated because of using the 527°C $S(\alpha, \beta)$ library at each temperature by approximately 19°C [20 MW(thermal)] and 30°C [40 MW(thermal)]. Keeping the coolant channel heat transfer coefficient constant causes an overestimation of 138°C.

V.B. Burnup

Depending on the core design, the maximum fuel temperature can increase with burnup because of axial power flattening. To explore the behavior of the current HTGR design, we analyze the power and temperature distributions over time. First, we verify that the design can reach 20 EFPY without refueling. Figure 13 shows k over time. No ^{10}B reactivity compensation was included here, and the graphite density was lowered to 1.74 g/cm³ to be more conservative (k_{eff} and lifetime increase with graphite density). The multiplication factor drops below 1 after 20.8 EFPY, or 115 GWd/t HM.

Since the core design is in the preliminary stage in this paper, the core temperature was kept at $T = 527^\circ\text{C}$ homogeneously. However, to assess the sensitivity of k_{eff} to the core temperature distribution, the burnup study was rerun with a more realistic (but exaggerated) temperature distribution. The fuel assembly layer temperatures were set to (top to bottom) 172°C, 527°C, 927°C, and 1372°C. The sensitivity study showed that the core lifetime slightly (+0.9 yr)

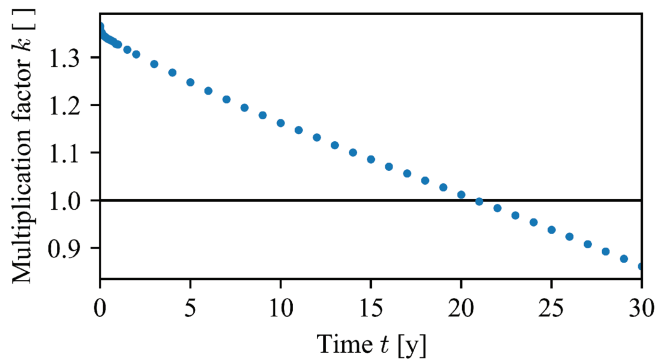


Fig. 13. Multiplication factor k over time during burnup of the 30×4 design.

increases with this temperature distribution, even if the average temperature is 200°C higher than for the homogeneous test case. This is due to the temperature coefficient of reactivity becoming stronger with decreasing temperatures.

Next, the maximum temperature and power density during burnup were analyzed. Table VI shows the results. Although axial flattening of the power density was observed, the maximum fuel temperature decreased with burnup. Figure 14 helps explain why. The power density calculated by Serpent as a function of x (at $z = 200$ cm) is plotted, with only the radial effects shown (axial burnup effects were normalized out). Both power profiles flatten, shifting power from the inner ring toward the outer ring of the fuel assemblies. Note that since the isotopic concentrations were tracked per fuel block, in-block flattening is stronger in reality than depicted here. Other axial planes show similar behavior.

V.C. Depressurized Loss of Forced Cooling

The DLOFC is generally considered one of the most severe incident scenarios, and we compare the results for

TABLE VI
Maximum Temperature and Power Density Peaking During Burnup

Burnup (yr)	ΔT_{max}^{fuel} (°C)	$\Delta P'''_{max}/P'''_{max}$
0	Reference	Reference
5	-41	-7.7%
10	-74	-15.5%
15	-103	-19.1%
20	-129	-23.9%

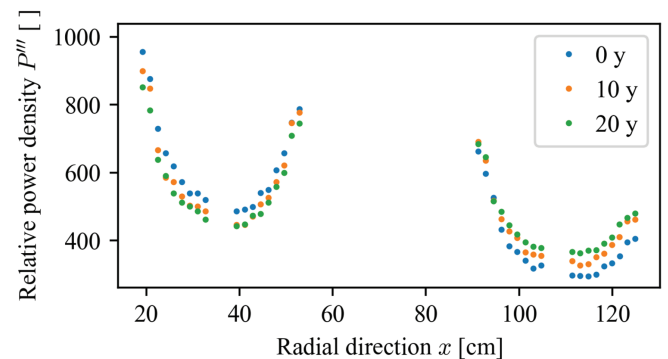


Fig. 14. Power density over time in the $z = 200$ cm plane. Only radial effects are shown; axial effects were normalized out.

two steady-state powers: 20 and 40 MW(thermal). The balance between decay heat power and core heat removal plays an important role. After the instantaneous loss of forced cooling, the only route for core decay heat removal is conduction through the core, thermal radiation from the barrel to the RPV, and conduction to the outer surface of the concrete, where it reaches the boundary fixed at 30°C.

Figure 15 shows the temperatures during a DLOFC. The top figure shows the overall maximum temperatures, and the bottom figure shows the core and fuel average temperatures. When the cooling stops, fuel temperatures increase initially. The fission power starts dropping, and thermal conductivity takes over at the timescale of conduction between fuel and coolant (~10 s). The overall maximum temperatures are quickly reached: 1185.0°C (+16.2°C) after 33s for the 20-MW(thermal) case, and 1457.0°C (+40.3°C) after 43s for the 40-MW(thermal) case. In Fig. 15, a small peak is visible at the beginning.

Next, the fission power decreases further because of thermal feedback and drops below decay heat power after about 150 s. Figure 16 top shows the total thermal power generation, radiative heat flux over the gas gap and heat flux to the environment. The bottom figure shows the maximum barrel and RPV temperatures. The intermediate cooling phase starts: Heat diffuses from the moderator-fuel interfaces radially toward the center of the fuel assembly, and the maximum temperature decreases at the timescale of conduction

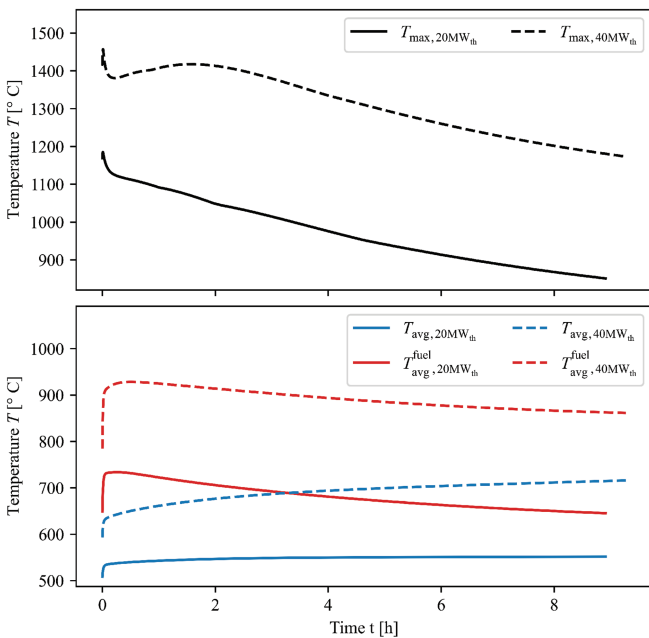


Fig. 15. The maximum temperature (top) and average temperatures of the whole core and fuel (bottom) of 20 and 40 MW(thermal) compared during a DLOFC.

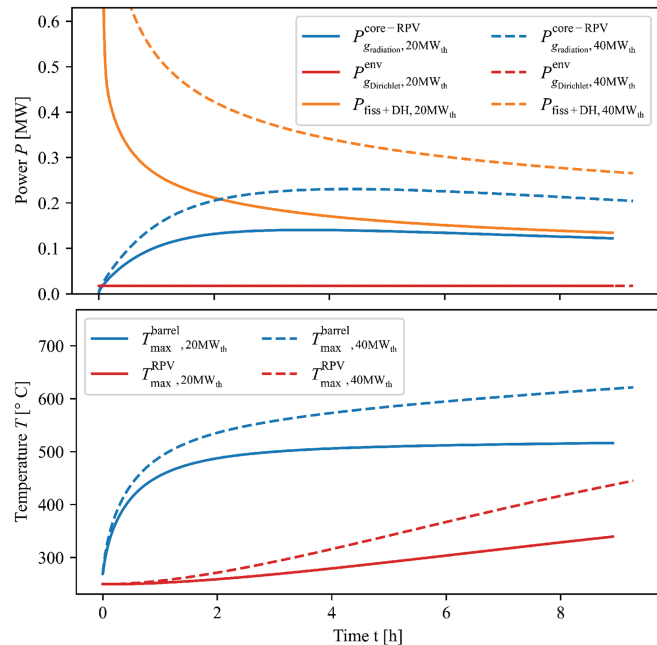


Fig. 16. Top: Total thermal power generation of 20 and 40 MW(thermal), heat flux from the core to the RPV, and heat flux to the Dirichlet boundary condition. Bottom: Maximum barrel and RPV temperatures.

within an assembly (~2000 s). While for the 20-MW(thermal) case, the maximum temperature continuously drops over time, the same does not hold for the 40-MW(thermal) case. There, an imbalance between decay heat generation and core heat removal initiates the core heatup phase. The maximum temperature reaches a second peak, $T_{max} = 1417.4^\circ\text{C}$. Finally, the behavior is determined by the balance between decay heat power and thermal diffusion rate. The two designs diverge in behavior and will be discussed in turn.

The most conservative understanding of safe shutdown during a DLOFC is that both maximum and average temperatures must be decreasing. This poses the questions: What is the maximum fuel temperature during the core heatup phase, and when is the safe shutdown phase reached? A complicating factor in a passive shutdown is the decay of ^{135}Xe : Fuel temperature must rise sufficiently to compensate for the reactivity insertion due to the decay of ^{135}Xe .

During the 20-MW(thermal) DLOFC, the average fuel temperature reaches its maximum 15 min after the onset of the incident and continuously decreases afterward. After 8.8 h, the reactor becomes recritical because of the combination of ^{135}Xe decay and fuel temperature cooling. Figure 17 shows the power and temperature during the first power peak. The increase in maximum temperature is limited to 38.4°C before the fuel reactivity feedback reduces the fission power density and heat

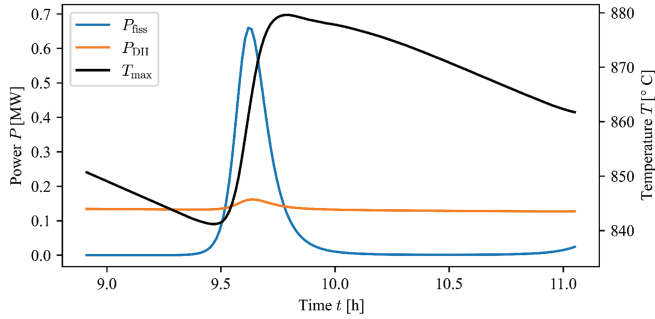


Fig. 17. The 20-MW(thermal) first recriticality event fission and decay heat powers and maximum fuel temperature.

diffusion takes over again. To reach safe shutdown in the conservative sense, the code would have to run until the heat flux at the 30°C boundary sink is larger than the core power production (after ~ 1000 h).

Each individual recriticality peak is on the order of ~ 1 h and requires many smaller time steps. It therefore takes long to fully resolve this event, requiring approximately 1×10^5 time steps. However, we can estimate the long-term behavior. All steady-state negative ^{135}Xe reactivity of -322 pcm has to be compensated, which translates to an expected $T_{avg}^{fuel} = 772.6^\circ\text{C}$. The reactor power to sustain this temperature without cooling will remain at least an order of magnitude below steady-state power, and assuming linearity, we estimate that $T_{max} < 838.0^\circ\text{C}$. The overall maximum temperature is therefore expected to be reached 30s after the onset of the incident and remain well below the safety limit of 1600°C .

Figure 18 illustrates the 40-MW(thermal) DLOFC long-term behavior. The figure shows the maximum temperature peaking a third time ($t = 408$ h, 1433°C) due to the sizable thermal barrier (1 m of concrete) separating the core from the environment heat sink. The heat sink flux exceeds decay heat power only after 482 h, and the ^{135}Xe concentration then is approximately $0/\text{cm}^3$, resulting in a positive $+527$ pcm reactivity insertion. Recriticality was not yet reached when the simulations were stopped but will be reached at an average fuel temperature of $T_{avg}^{fuel} \approx 1006^\circ\text{C}$. Following the same line of reasoning as the 20-MW(thermal) case, $\lim_{t \rightarrow \infty} T_{max} < 1414^\circ\text{C}$.

Finally, we discuss the barrel and RPV temperatures. The heat flux out of the core is inhibited by the concrete encasement, and the simplification that axial and tangential thermal conductivities are 0 further worsened heat transfer. Figure 18 shows that the maximum RPV and barrel temperatures reach a peak temperature of approximately 1220°C [40-MW(thermal)

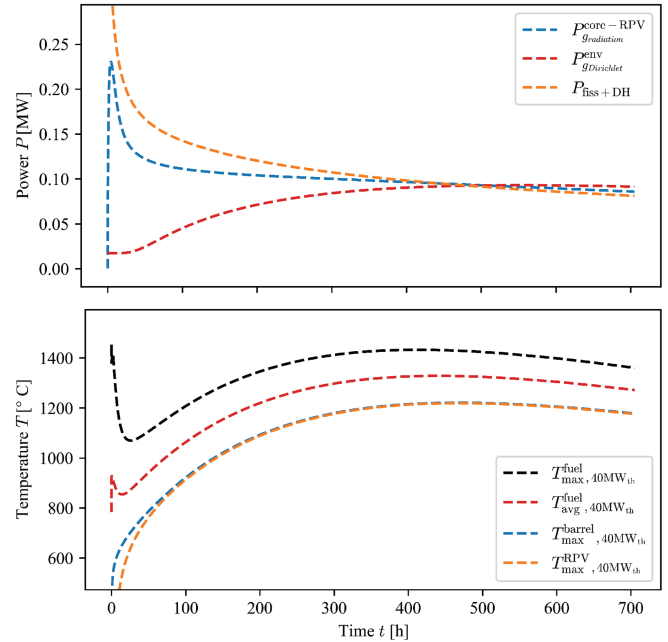


Fig. 18. Top: The 40-MW(thermal) long-term total thermal power generation, heat flux from the core to the RPV, and heat flux to the Dirichlet boundary condition. Bottom: The maximum fuel, barrel, and RPV temperatures and the average fuel temperature.

DLOFC]. In both the 20-MW(thermal) case and the 40-MW(thermal) case, the limit RPV temperature (395°C for steady state and 445°C for several hours during incidents) is significantly breached. For the 20-MW(thermal) case, it could possibly suffice to include better thermal insulation around the core. For the 40-MW(thermal) design, an RCCS must be adopted to enable sufficient cooling.

V.D. Partial Blockage

Figure 19 shows the maximum temperature, average fuel temperature, and total power of the reactor during two partial blockage events. In the first minute, the average and maximum fuel temperatures increase as a result of the loss of cooling, leading to a drop in fission power. The initial drop in fission power reaches a plateau after 2 min at approximately 95% (one block stack) and 85% (three block stacks) of steady-state power. However, the maximum temperature continues to increase to more than 2300°C without a sign of stabilizing. Figure 20 shows the temperature distribution throughout the core at $t = 100$ s and at $t = 500$ s.

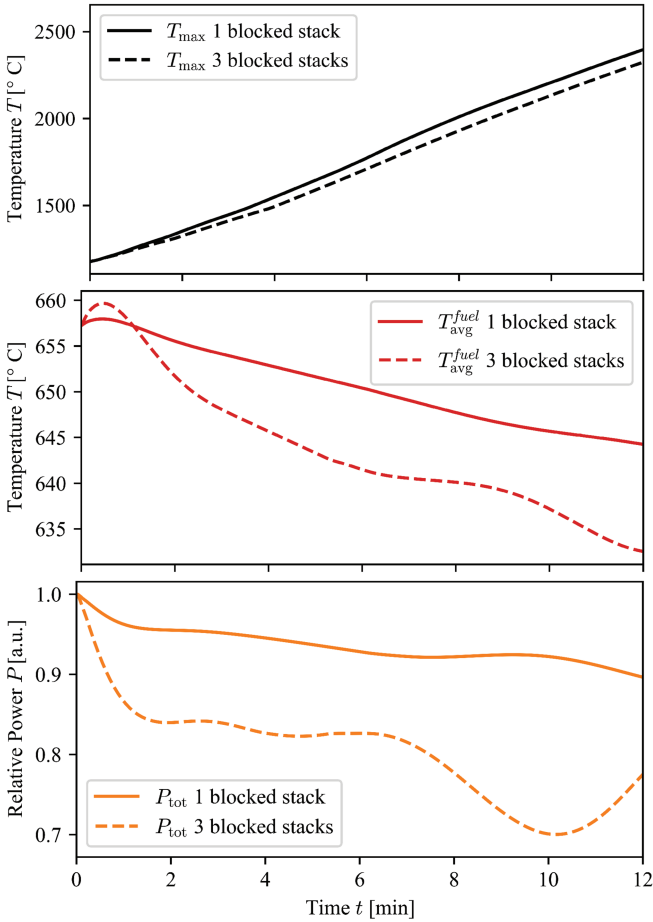


Fig. 19. Maximum temperature (top), average fuel temperature (middle), and total power (bottom) during a partial blockage.

Different competing mechanisms influence the behavior after 100 s. The average fuel temperature decreases further, adding positive reactivity. However, increasing

temperature in the blocked assemblies causes a negative reactivity insertion. While the temperature coefficient of reactivity decreases with temperature (see Sec. III.B), the central fuel blocks’ cross sections are of higher importance to the effective multiplication factor. Therefore, the temperature increase at the core center has a relatively large impact.

The maximum allowable temperature of 1600°C is severely exceeded by at least 793°C (one blocked stack) and 729°C (three blocked stacks), with temperatures still rising after the termination of the simulations. In addition, the current simulations assumed that the mass flux through the remaining unblocked coolant channels remained unchanged. If the coolant flow instead increases in those coolant channels while keeping the total mass flux equal, another possibly more severe scenario may be obtained.

Therefore, it is important that a partial blockage incident be detected in time. Several detection options exist. The average helium outlet temperature starts to decrease from the onset of the blockage: When the 1600°C fuel temperature limit is reached, the helium temperature dropped by 14°C (one blocked stack) and 53°C (three blocked stacks). Local coolant outlet temperature measurements are more sensitive to the incident: After 500 s, the maximum single helium outlet temperature has increased +219°C (one blocked stack) and +115°C (three blocked stacks). Another option is to compare tangential differences in neutron flux. Figure 21 plots the relative difference in fast-group scalar flux over x at $y=0$ cm and $z=200$ cm compared to steady state, 500 s into the partial blockage event of one blocked stack. The fast-group scalar flux difference outside the core between the left and right sides amounts to 3.4%.

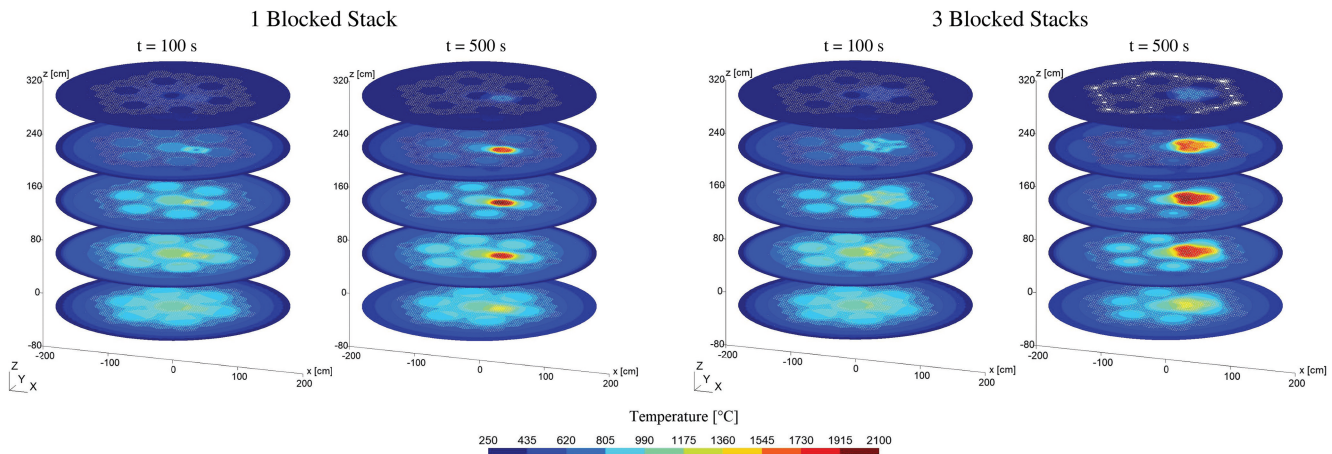


Fig. 20. The temperature distribution at $t = 100$ s and $t = 500$ s during a partial blockage incident, with one (left two figures) or three (right two figures) blocked stacks.

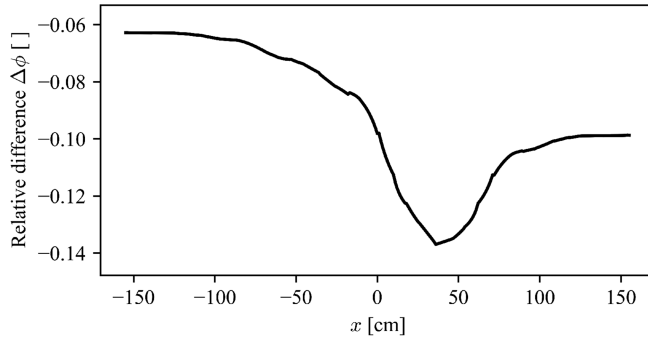


Fig. 21. Relative difference in fast-group scalar flux between steady state and $t = 500$ s into a single blocked assembly incident at $y = 0$ cm, $z = 200$ cm.

The simplifications in modeling the power conversion system will most likely cause a more direct temperature feedback to the core inlet temperature. While the core helium outlet temperature increases, the core inlet temperature decreased because of the lowered mass flux, allowing the heat exchanger to further cool the primary circuit helium. The faster temperature feedback may have slightly increased the core power during the partial blockage, leading to an overestimation of the maximum temperature. The heat exchanger simplifications are therefore conservative in simulating the partial blockage. However, more sensitivity analyses, for example, changing the mass flux or hot and cold duct delay times, could provide useful information on feedback.

This research should be repeated especially in larger cores. Both changes in pressure drop and mass flux will remain smaller there, as well as the relative tangential difference in scalar flux outside the core. For example, the GT-MHR (see Ref. [19] for details) has 120 fuel assemblies per layer; a blocked stack would mean that 0.8% of the channels are blocked. Moreover, if one of the central fuel assemblies is blocked, the radial distance to the active core side is larger, so that tangential flux differences will be smaller.

V.E. Bypass Flow

Core bypass flow between the prismatic fuel assemblies is a result of gaps between the blocks. An initial gap size of minimally 1 mm is necessary for assembling the core. But, the gap width will increase over time as a result of irradiation-induced graphite shrinkage. Neglecting bypass flow is an unavoidable simplification of 2D core geometry modeling

and was neglected in the current model too. Yet, it can result in a significant underestimation of the maximum fuel temperature. For example, Tak et al.^[26] presented a high-resolution (e.g., using a 70 times finer mesh) computational fluid dynamics (CFD) model of 1/12th of a fuel assembly stack of 10 blocks. Assuming a uniform power profile of 31 W/cm^3 , they reported a maximum fuel temperature underestimation of more than 60°C if bypass flow is neglected. Sato et al.^[44] modeled the same reactor but report a more severe increase of 138°C when the axial power profile and radial power peak factor are also taken into account.

However, the literature CFD models do not include the sharp power density peaks we observed at fuel-reflector boundaries. Huning et al.^[4] include a thorough analysis of bypass gap width on the maximum temperature. However, the thermal-hydraulic code assumed a radially uniform power density distribution. The question therefore remains whether the bypass flow increases the maximum fuel temperature when increasing the power peaking.

To estimate the effect, we first obtained a fit of the power density distribution in the first fuel block stack right of the center (the same assembly that was blocked during the single blocked stack incident; see Fig. 9). We fitted the distribution in x and z separately and assumed that $P'''(y)$ is constant (the variations are an order of magnitude smaller than in x), obtaining $P'''(\vec{r}) = P'''(x) \cdot P'''(z)$. We conservatively ran PHANTOM-S_N at a uniform temperature of 527°C to find $P'''(\vec{r})$, which further increased radial and axial power peaking due to the lack of thermal feedback. In the axial dimension, a cosine shape is found that reverses close to the top and bottom reflectors because of the enhanced neutron thermalization and limited axial resolution of the mesh. Next, we ran a single-stack geometry in OPERA with the obtained power density fit and updated the total power until the same maximum temperature was reached as in full-core simulations. The final power density fit

$$P'''(z) \approx \begin{cases} \cos\left(\frac{(z+280)-160}{160} \cdot \frac{\pi}{2}\right) \cdot 5.5 + 5 & z < 20\text{cm} \\ \cos\left(\frac{(z-160)}{160} \cdot \frac{\pi}{2}\right) \cdot 5.5 + 5 & 20\text{cm} < z < 300\text{cm} \\ \cos\left(\frac{(z-280)-160}{160} \cdot \frac{\pi}{2}\right) \cdot 5.5 + 5 & z > 300\text{cm} \end{cases} \quad (13)$$

describes the axial shape, and

$$P'''(x) \approx 1.49 \times 10^{-5} \cdot x^4 - 4.79 \times 10^{-5} \cdot x^3 - 5.36 \times 10^{-4} \cdot x^2 + 1.72 \times 10^{-3} \cdot x - 8.44 \times 10^{-1} \quad (14)$$

shows the distribution of the power in x . Here, both x and z are in units of centimeters, and all P''' are in units of W/cm^3 . Figure 22 shows the fit in z and x . Compared to the $z = 12$ cm plane in the whole-core model, the largest temperature difference is approximately $50^\circ C$.

The bypass flow is modeled as “stolen” from the coolant channels, meaning that the total mass flux remains equal. Table VII shows the bypass flow fraction, the maximum fuel temperature, the maximum coolant outlet temperature, and the average bypass flow exit temperature.

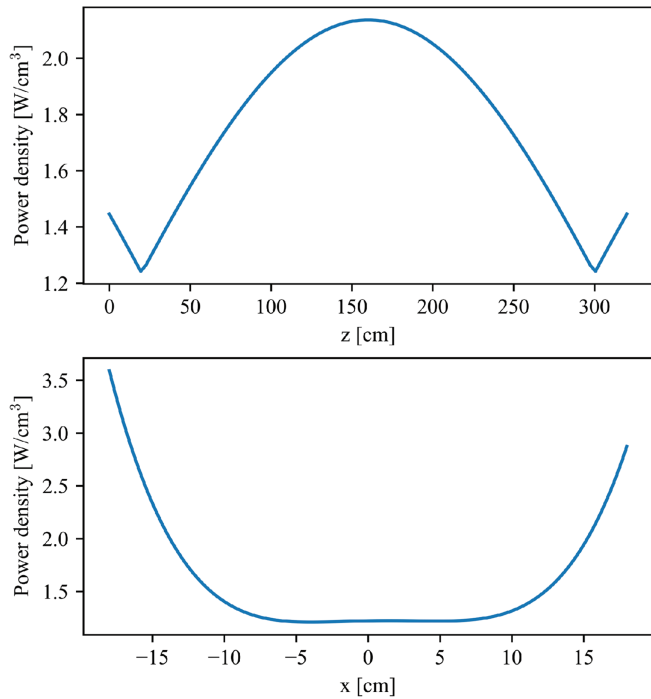


Fig. 22. Fit in z and x of the power density distribution in the fuel assembly stack just right of the center.

Figure 23 shows the temperature distribution in the plane $z = 12$ cm, where the highest temperature was found. Two distributions are shown: one for no bypass flow and one for maximal simulated bypass flow (15%).

In contrast to what is reported in literature,^[4,26,44] the results show that the bypass flow will lower the maximum temperature for the current design. Of course, the model used here is limited in its spatial resolution compared to the high-fidelity CFD models employed by Tak et al.^[26] and Sato et al.^[44] Nevertheless, it includes an important aspect of HTGRs such as the modular high-temperature gas-cooled reactor (MHTGR) and the current design, which is the block boundary power peaking that is observed at the fuel-reflector interface (for another whole-core code showing the power peaking, see Ref. [3]). In the micro HTGR modeled here, the peaks are exacerbated by the high fissile fuel content needed to reach a 20-yr lifetime, adding to the effect. These effects can accurately be captured only when a representative core part is modeled, including multiple fuel assemblies and reflector assemblies and a power density that is derived from coupled simulations. Bypass flows such as flow around control rods, between reflector assemblies at the sides of the reactor, and assembly cross flow are neglected since these effects are expected to be small.^[45]

V.F. Reactivity Insertion

The ejection of a control rod may unintentionally insert reactivity into the system and is a design-basis accident. In an HTGR, reactivity may also be inserted when water ingresses the active core coolant channels, as the core is strongly undermoderated. This event is particularly probable when a Rankine power conversion cycle is adopted in the secondary loop.

We first researched the maximum reactivity insertion possible as a function of uniform water density in the core coolant channels. Figure 24 plots the reactivity ρ_{WT} (pcm) introduced against the water density. The figure

TABLE VII

Bypass Sensitivity Analysis Results Using a Power Density Fit

Flow Fraction (%)	0	0.5	1.0	2.0	5.0	10.0	15.0
Maximum fuel temperature ($^\circ C$)	1168	1166	1163	1159	1145	1120	1099
Maximum coolant outlet temperature ($^\circ C$)	985	985	984	983	977	964	952
Maximum bypass outlet temperature ($^\circ C$)	250	920	921	924	949	970	962
Average bypass outlet temperature ($^\circ C$)	250	847	847	848	860	861	839

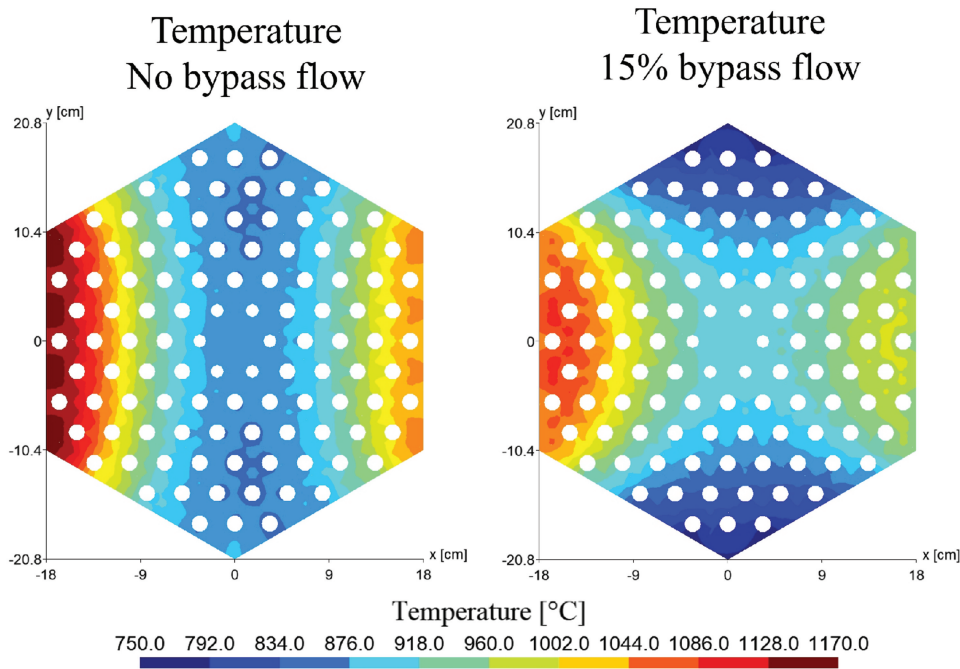


Fig. 23. The temperature distribution at $z = 12$ cm with no bypass flow and 15% stolen bypass flow modeled in the fuel assembly stack just right of the middle.

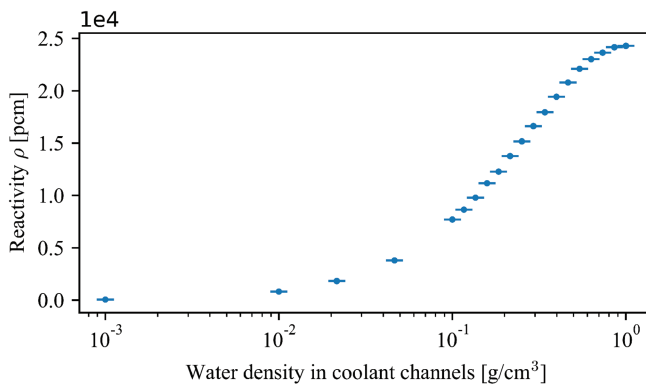


Fig. 24. Reactivity increase as a function of coolant channel water density.

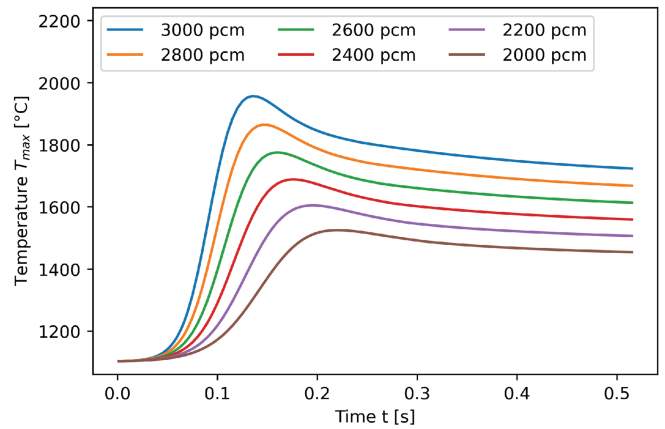


Fig. 25. Maximum temperature during a reactivity insertion incident.

shows that a maximum reactivity insertion of 2.4×10^4 pcm (37 \$) is reached when the water density is 1 g/cm^3 . The additional reactivity is especially high in this reactor because of its high fuel content.

The system can compensate for some reactivity insertion through temperature feedback. To find the maximum amount, a sensitivity analysis was first performed in a simplified single-stack geometry. The single stack was modeled with reflective boundary conditions on the sides and the average power density of the 20-MW(thermal) whole core. Figure 25 shows the maximum temperature as a function of time for several different reactivity

insertion amounts, ranging from 2000 to 3000 pcm. During the 2200 pcm reactivity insertion, the maximum temperature remains just below 1600°C .

Next, the reactivity insertion incident is modeled in the whole core. Figure 26 shows the total power and the maximum and average fuel power of the simulation for the first 2.5 s after an instantaneous reactivity insertion. Reactivity increases of 1000 pcm and 2000 pcm were modeled to compare the results. The maximum fuel temperature reaches 1972°C (1000 pcm) and exceeds the

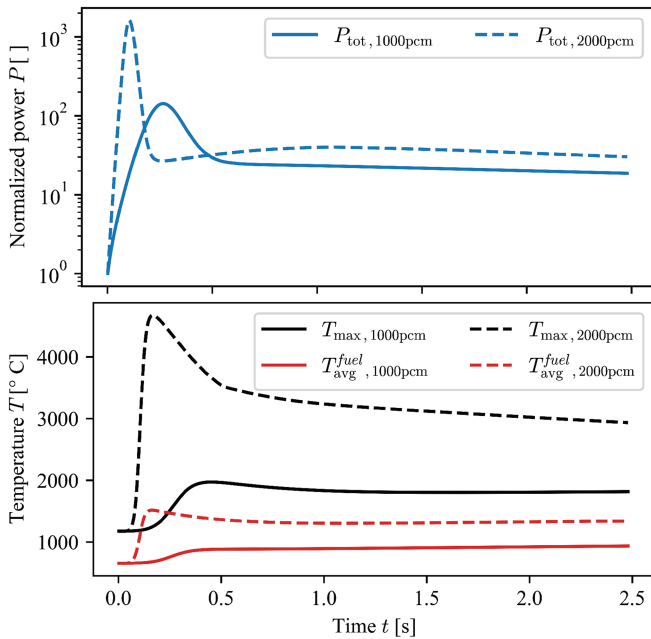


Fig. 26. Total power (top figure, logarithmic y scale, normalized for steady-state power) and maximum and average fuel temperature (bottom figure) during the first 2.5 s for 1000 and 2000 pcm instantaneous reactivity insertion incidents.

design limit. Again, the fuel block boundary power peaking caused a much greater increase in temperature than could be expected from the simplified infinite-lattice calculations. A 1000 pcm reactivity insertion corresponds to 0.012 g/cm³.

To put that into perspective, we may compare it with Ref. [46]. Zheng et al. modeled a water ingress incident in a HTR-PM reactor and indicate that 600 kg of water ingresses into the 400-m³ primary circuit before the primary and secondary circuit pressures are in equilibrium. This corresponds to a water density of 0.0015 g/cm³, which would lead to a much smaller reactivity insertion.

The timescales show that using a unit-cell model would underestimate the temperature. In unit-cell models, the fuel pin and surrounding graphite temperatures are homogenized. The subpin temperature distribution would not be resolved, and the heat capacity of the surrounding graphite would be added to that of the fuel pin. The timescale for heat conduction from the fuel pin to the surrounding graphite is ~ 1 s, whereas Figs. 25 and 26 show that the temperature peak is reached within 0.25 s for a 2000 pcm insertion. The same might be argued for the homogenization of the TRISO particles, but the timescale of heat conduction from the TRISO kernel center to the surrounding graphite compact material is in the order of 0.02 s.

Three factors complicate drawing final conclusions about the water ingress incident. First, the reactivity insertion was modeled instantaneously. In reality, the reactivity insertion is delayed (see, e.g., Ref. [46] for more information), decreasing the peak power and maximum temperature.

Second, the reactor inlet temperature co-determines the average and maximum fuel temperatures during a reactivity insertion incident, for which a simplified model was currently used. We tested the sensitivity of the system by varying the coolant transport times through the hot and cold ducts and the intermediate heat exchanger and simulating the single-stack geometry. The times were set at 1 and 10s for each of the components (3 and 30s in total). Figure 27 displays the maximum temperatures for the different settings, showing that the difference in maximum temperature is around 1°C.

On the other hand, the whole-core simulation reaches the maximum temperature after 0.5 s. The coolant loop model does not in any way influence this peak temperature. However, for the new steady-state fuel temperature, the model could benefit from a more thorough sensitivity analysis. The important parameters include the heat-exchanging surface area and the secondary circuit's temperatures. Ideally, a 1D CFD model is added to include pressure and flow rate changes.

Finally, since the graphite heat capacity value was kept constant at cold conditions, the core temperature rise was overestimated. We tested the 1000 pcm reactivity insertion event again, including c_p as a function of temperature. The results indicated that the temperatures rise more slowly, causing a higher peak in total power P_{tot} by +287% but a lower maximum temperature of -184°C .

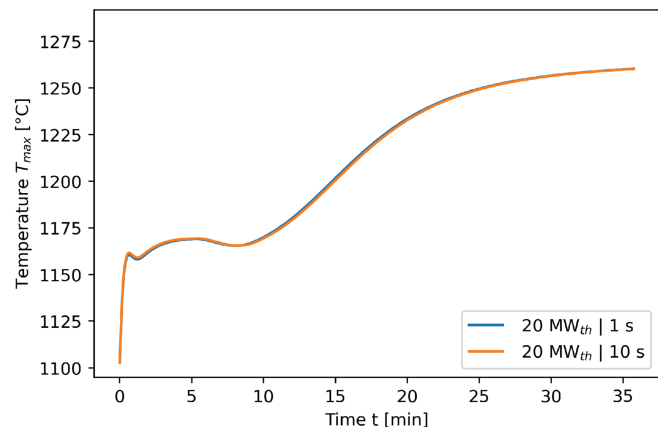


Fig. 27. Maximum fuel temperature during a reactivity insertion incident for 1- and 10-s coolant delays per each component.

VI. CONCLUSIONS AND FURTHER WORK

A whole-core transient coupled thermal-hydraulic and neutronics model was presented and tested on a prismatic micro HTGR. We are not aware of any other documented attempt on the coupled transient whole-core modeling of HTGR transients, especially so with subpin temperature resolution and near-pin neutronics resolution. Irradiation temperature-dependent graphite thermal conductivity was included, which can severely deteriorate as a result of accumulating radiation damage at low graphite temperatures. The whole-core model is able to model asymmetric transients. A partial blockage was simulated to test the inherent safety of the reactor during more complex incidents.

The model leads us to two important conclusions. First, while the DLOFC is generally seen as one of the most severe incidents, a partial blockage event may be more severe when it comes to fuel temperature limits being exceeded. Indeed, the temperature feedback of the entire core during a DLOFC is able to quickly reduce the fission power. During a partial blockage, the reactor does not passively shut down; instead, fission power is only reduced. This continued operation causes the maximum fuel temperature to rise above 2300°C when a single fuel assembly is blocked. Future work may include studying different core designs that might lower the impact of a partial blockage scenario and researching what minimal number of blocked channels leads to temperatures exceeding design limits.

Second, the combination of subpin temperature distribution with temperature and irradiation temperature-dependent thermal conductivity introduces a more accurate estimate of the temperature distribution in the core. Previous models included only fluence or temperature-dependent thermal conductivities. In reality, irradiation temperature is the most important parameter, causing a decrease in conductivity of up to 97%. The subpin temperature distribution is important in accurately computing both the fuel pin and the graphite block webbing temperature. When these are homogenized, the graphite temperature may be overestimated, which in turn can lead to an overestimation of the thermal conductivity. In the future, we plan on including a model for graphite annealing: When the temperature increases during a transient, irradiation-induced graphite damage can be repaired, and the thermal conductivity can return to unirradiated values.

The new model poses new opportunities in modeling small modular prismatic HTGRs. It is especially adept at accurately modeling the temperature distribution during

asymmetric transients in coupled simulations. These coupled simulations enable the demonstration of inherent safety during all imaginable thermal-hydraulic or neutronics-related incidents. If a core can be designed for which the passive safety is exhaustively proved, this may be a great opportunity for the future energy supply.

Disclosure Statement

No potential conflict of interest was reported by the author(s).

ORCID

Marc C. Van Den Berg  <http://orcid.org/0000-0001-6810-3717>

Danny Lathouwers  <http://orcid.org/0000-0003-3810-1926>

References

1. F. J. WOLS et al., “Conceptual Design of a Passively Safe Thorium Breeder Pebble Bed Reactor,” *Ann. Nucl. Energy*, **75**, 542 (2015); <https://doi.org/10.1016/J.ANUCENE.2014.09.012>.
2. K. J. CONNOLLY et al., “A Coarse-Mesh Coupled Neutronics and Thermal Fluids Method for Prismatic Cores,” *Nucl. Sci. Eng.*, **184**, 2, 228 (2016); <https://doi.org/10.13182/NSE15-105>.
3. A. HUNING, S. CHANDRASEKARAN, and S. GARIMELLA, “Whole-Core Transient Analysis Methodology for Prismatic High Temperature Gas Reactors,” *Nucl. Eng. Des.*, **368**, 110788 (2020); <https://doi.org/10.1016/J.NUCENGDES.2020.110788>.
4. A. J. HUNING, S. GARIMELLA, and F. RAHNEMA, “A Steady-State Thermal-Hydraulic Analysis Method for Prismatic High-Temperature Gas-Cooled Reactors,” *Nucl. Technol.*, **193**, 2, 234 (2016); <https://doi.org/10.13182/NT15-14>.
5. N. STAUFF and C. H. LEE, “Core Design of the Holos-Quad Microreactor,” ANL/NSE-22/4, Argonne National Laboratory (2022); <https://publications.anl.gov/anlpubs/2022/04/173835.pdf>.
6. A. BERENS et al., “Multiphysics Analysis of PLOFC and DLOFC Accidents in the HTGR-TR,” *Nucl. Technol.*, **210**, 10, 1824 (2024); <https://doi.org/10.1080/00295450.2024.2302723>.
7. C. FILIPPONE, “Preliminary Thermal-Hydraulics and Selected Safety Analysis for Holos-Quad Reactor Design,” ANL-NSE-22/1, Argonne National Laboratory

- (2022); <https://publications.anl.gov/anlpubs/2022/04/174551.pdf>.
8. B. MAYES et al., “Sensitivity of SC-HTGR Conduction Cooldown to Reactor Cavity Cooling System Failure,” *Nucl. Technol.*, **208**, 8, 1311 (2022); <https://doi.org/10.1080/00295450.2021.1947664>.
 9. A. SEUBERT et al., “The Transient 3-D Transport Coupled Code TORT-TD/ATTICA3D for High-Fidelity Pebble-Bed HTGR Analyses,” *Transp. Theory Stat. Phys.*, **41**, 1–2, 133 (2012); <https://doi.org/10.1080/00411450.2012.671212>.
 10. A. SEUBERT et al., “The 3-D Time-Dependent Transport Code TORT-TD and Its Coupling with the 3D Thermal-Hydraulic Code ATTICA3D for HTGR Applications,” *Nucl. Eng. Des.*, **251**, 173 (2012); <https://doi.org/10.1016/j.nucengdes.2011.09.067>.
 11. S. BAIER et al., “Extension and Application of the Reactor Dynamics Code DYN3D for Block-Type High Temperature Reactors,” *Nucl. Eng. Des.*, **271**, 431 (2014); <https://doi.org/10.1016/j.nucengdes.2013.12.013>.
 12. G. HAAG, “Forschungszentrum Jülich Properties of ATR-2E Graphite and Property Changes Due to Fast Neutron Irradiation,” Forschungszentrum Jülich in der Helmholtz-Gemeinschaft (2005).
 13. H. J. RÜTTEN, K. A. HAAS, and C. POHL, “Computer Code System V.S.O.P. (99/11) Update 2011 of V.S.O.P. (99)-Version 2009 CODE MANUAL,” Forschungszentrum Jülich (2011).
 14. J. KÓPHÁZI and D. LATHOUWERS, “Three-Dimensional Transport Calculation of Multiple Alpha Modes in Subcritical Systems,” *Ann. Nucl. Energy*, **50**, 167 (2012); <https://doi.org/10.1016/J.ANUCENE.2012.06.021>.
 15. J. LEPPANEN et al., “The Serpent Monte Carlo Code: Status, Development and Applications in 2013,” *Ann. Nucl. Energy*, **82**, 142 (2015); <https://doi.org/10.1016/J.ANUCENE.2014.08.024>.
 16. M. DING et al., “Design of a U-Battery®,” Delft University of Technology (2011).
 17. J. W. STERBENTZ et al., “High-Temperature Gas-Cooled Test Reactor Point Design,” INL/EXT-16-38296, Idaho National Laboratory (2016); <https://inldigitallibrary.inl.gov/sites/sti/sti/6899493.pdf>.
 18. C. WANG, “Design, Analysis and Optimization of the Power Conversion System for the Modular Pebble Bed Reactor System,” Massachusetts Institute of Technology (2003).
 19. “GT-MHR Conceptual Design Description Report Reference: NRC Project No. 716,” General Atomics (1996); <https://www.nrc.gov/docs/ML0224/ML022470282.pdf>.
 20. M. DING and J. L. KLOOSTERMAN, “Thermal-Hydraulic Design and Transient Evaluation of a Small Long-Life HTR,” *Nucl. Eng. Des.*, **255**, 347 (2013); <https://doi.org/10.1016/j.nucengdes.2012.11.009>.
 21. J. VERRUE, M. DING, and J. L. KLOOSTERMAN, “Thorium Utilisation in a Small Long-Life HTR. Part III: Composite-Rod Fuel Blocks,” *Nucl. Eng. Des.*, **267**, 253 (2014); <https://doi.org/10.1016/j.nucengdes.2013.08.075>.
 22. C. GEUZAINÉ and J.-F. REMACLE, “Gmsh: A Three-Dimensional Finite Element Mesh Generator with Built-In Pre-and Post-Processing Facilities,” *Int. J. Numer. Meth. Eng.*, **79**, 11, 1309 (2009).
 23. ANSI/ANS-5.1-1993, *Decay Heat Power in Light Water Reactors*, American Nuclear Society, Westmont, Illinois (1993).
 24. L. MASSIMO, *Physics of High-Temperature Reactors*, Pergamon Press (1976).
 25. D. N. ARNOLD, “An Interior Penalty Finite Element Method with Discontinuous Elements,” **19**, 4, 742 (1982); <https://doi.org/10.1137/0719052>.
 26. N.-I. TAK, M.-H. KIM, and W. J. LEE, “Numerical Investigation of a Heat Transfer Within the Prismatic Fuel Assembly of a Very High Temperature Reactor,” *Ann. Nucl. Energy*, **35**, 10, 1892 (2008); <https://doi.org/10.1016/j.anucene.2008.04.005>.
 27. F. MIFTASANI et al., “Investigating Geometry Adjustments for Enhanced Performance in a PeLUIt-10 MWt Pebble Bed HTGR with OTTO Refueling Scheme,” *Nucl. Eng. Des.*, **422**, 113163 (2024); <https://doi.org/10.1016/J.NUCENGDES.2024.113163>.
 28. M. ROSS et al., “Passive Heat Removal in Horizontally Oriented Micro-HTGRs,” *Prog. Nucl. Energy*, **156**, 104530 (2023); <https://doi.org/10.1016/J.PNUCENE.2022.104530>.
 29. A. J. NOVAK et al., “Pronghorn Theory Manual,” Idaho National Laboratory (2020).
 30. Y. ZHENG et al., “Study on the DLOFC and PLOFC Accidents of the 200 MWe Pebble-Bed Modular High Temperature Gas-Cooled Reactor with TINTE and SPECTRA Codes,” *Ann. Nucl. Energy*, **120**, 763 (2018); <https://doi.org/10.1016/j.anucene.2018.06.041>.
 31. B. BOER, “Optimized Core Design and Fuel Management of a Pebble-Bed Type Nuclear Reactor,” PhD Thesis, Delft University of Technology (2009).
 32. B. KELLY, “The Thermal Conductivity of Graphite,” *Chemistry and Physics of Carbon*, Vol. 5, p. 119, Marcel Dekker, New York (1969).
 33. G. HAAG, “Thermal Conductivity of Graphite Irradiated with Medium and High Neutron Fluences,” Forschungszentrum Jülich (2003).
 34. B. KELLY, “Irradiation Damage in Graphite Due to Fast Neutrons in Fission and Fusion Systems,” International Atomic Energy Agency (2000).

35. M. GLADYSHEV, F. REITSMA, and T. YASAR, “IAEA Nuclear Graphite Knowledge Base,” International Atomic Energy Agency (2015); https://www.iaea.org/resources/data_bases/iaea-nuclear-graphite-knowledge-base.
36. D. MCELIGOT et al., “Thermal Properties of G-348 Graphite,” INL/EXT-16-38241, Idaho National Laboratory (2016); <http://www.osti.gov/servlets/purl/1330693/>.
37. Y. C. CHIEW and E. D. GLANDT, “The Effect of Structure on the Conductivity of a Dispersion,” *J. Colloid Interface Sci.*, **94**, 1, 90 (1983); [https://doi.org/10.1016/0021-9797\(83\)90238-2](https://doi.org/10.1016/0021-9797(83)90238-2).
38. E. E. GONZO, “Estimating Correlations for the Effective Thermal Conductivity of Granular Materials,” *Chem. Eng. J.*, **90**, 3, 299 (2002); [https://doi.org/10.1016/S1385-8947\(02\)00121-3](https://doi.org/10.1016/S1385-8947(02)00121-3).
39. R. STAINSBY et al., “Investigation of Local Heat Transfer Phenomena in a Pebble Bed HTGR Core,” AMEC NSS Limited (2009).
40. H. NABIELEK, Personal Communication (2024).
41. Y. H. TUNG, R. W. JOHNSON, and H. SATO, “Effects of Graphite Surface Roughness on Bypass Flow Computations for an HTGR,” *Nucl. Eng. Des.*, **252**, 78 (2012); <https://doi.org/10.1016/J.NUCENGDES.2012.07.010>.
42. “Design Features to Achieve Defence in Depth in Small and Medium Sized Reactors (No. NP-T-2.2),” International Atomic Energy Agency (2009).
43. A. BARSELL et al., “HTGR Accident Initiation and Progression Analysis Status Report. Volume VI. Event Consequences and Uncertainties Demonstrating Safety R&D Importance of Fission Product Mechanisms,” General Atomics (1976).
44. H. SATO et al., “Analysis of Core Heat Removal Capability Under DLOFC Accidents for HTGRs,” *Nucl. Eng. Des.*, **271**, 530 (2014); <https://doi.org/10.1016/j.nucengdes.2013.12.028>.
45. R. B. VILIM, W. D. POINTER, and T. Y. C. WEI, “Prioritization of VHTR System Modeling Needs Based on Phenomena Identification, Ranking and Sensitivity Studies,” Argonne National Laboratory (2006); <https://digital.library.unt.edu/ark:/67531/metadc886112/>.
46. Y. ZHENG, L. SHI, and Y. WANG, “Water-Ingress Analysis for the 200 MWe Pebble-Bed Modular High Temperature Gas-Cooled Reactor,” *Nucl. Eng. Des.*, **240**, 10, 3095 (2010); <https://doi.org/10.1016/j.nucengdes.2010.05.028>.